Acta Pharmaceutica Sinica B 2025;15(8):3997−4013

Chinese Pharmaceutical Association
Institute of Materia Medica, Chinese Academy of Medical Sciences

Acta Pharmaceutica Sinica B

www.elsevier.com/locate/apsb
www.sciencedirect.com

ORIGINAL ARTICLE

Augmentation of PRDX1−DOK3 interaction alleviates rheumatoid arthritis progression by suppressing plasma cell differentiation

Wenzhen Dang[a,b,e,†], Xiaomin Wang[c,†], Huaying Li[d,†], Yixuan Xu[b,e,†], Xinyu Li[a,e], Siqi Huang[b,e], Hongru Tao[a,b], Xiao Li[a,b], Yulin Yang[b], Lijiang Xuan[b], Weilie Xiao[i], Dean Guo[b], Hao Zhang[b], Qiong Wu[d], Jie Zheng[b], Xiaoyan Shen[f], Kaixian Chen[b], Heng Xu[b,e,*], Yuanyuan Zhang[b,e,*], Cheng Luo[a,b,c,e,g,h,*]

[a]*School of Pharmaceutical Science and Technology, Hangzhou Institute for Advanced Study, University of Chinese Academy of Sciences, Hangzhou 310024, China*
[b]*State Key Laboratory of Drug Research, Shanghai Institute of Materia Medica, Chinese Academy of Sciences, Shanghai 201203, China*
[c]*School of Chinese Materia Medica, Nanjing University of Chinese Medicine, Nanjing 210023, China*
[d]*MegaRobo Technologies Co., Ltd., Beijing 100085, China*
[e]*University of Chinese Academy of Sciences, Beijing 100049, China*
[f]*Department of Pharmacology and the Key Laboratory of Smart Drug Delivery Ministry of Education, School of Pharmacy, Fudan University, Shanghai 201203, China*
[g]*State Key Laboratory of Functions and Applications of Medicinal Plants, Guizhou Medical University, Guiyang 550014, China*
[h]*Zhongshan Institute for Drug Discovery, Shanghai Institute of Materia Medica, Chinese Academy of Sciences, Zhongshan 528437, China*
[i]*Key Laboratory of Medicinal Chemistry for Natural Resource, Ministry of Education, School of Pharmacy and School of Chemical Science and Technology, Yunnan University, Kunming 650500, China*

Received 23 January 2025; received in revised form 21 May 2025; accepted 23 May 2025

*Corresponding authors.
E-mail addresses: idaheng@simm.ac.cn (Heng Xu), zhangyy@simm.ac.cn (Yuanyuan Zhang), cluo@simm.ac.cn (Cheng Luo).
[†]These authors contributed equally to this work.
Peer review under the responsibility of Chinese Pharmaceutical Association and Institute of Materia Medica, Chinese Academy of Medical Sciences.

https://doi.org/10.1016/j.apsb.2025.06.006
2211-3835 © 2025 The Authors. Published by Elsevier B.V. on behalf of Chinese Pharmaceutical Association and Institute of Materia Medica, Chinese Academy of Medical Sciences. This is an open access article under the CC BY-NC-ND license (http://creativecommons.org/licenses/by-nc-nd/4.0/).

KEY WORDS

Rheumatoid arthritis;
Plasma cell;
PRDX1;
DOK3;
Degradation;
Interaction;
Salvianolic acid B;
Molecular glue

Abstract Rheumatoid arthritis (RA) is a chronic autoimmune disease characterized by persistent inflammation and joint damage, accompanied by the accumulation of plasma cells, which contributes to its pathogenesis. Understanding the genetic alterations occurring during plasma cell differentiation in RA can deepen our comprehension of its pathogenesis and guide the development of targeted therapeutic interventions. Here, our study elucidates the intricate molecular mechanisms underlying plasma cell differentiation by demonstrating that PRDX1 interacts with DOK3 and modulates its degradation by the autophagy−lysosome pathway. This interaction results in the inhibition of plasma cell differentiation, thereby alleviating the progression of collagen-induced arthritis. Additionally, our investigation identifies Salvianolic acid B (SAB) as a potent small molecular glue-like compound that enhances the interaction between PRDX1 and DOK3, consequently impeding the progression of collagen-induced arthritis by inhibiting plasma cell differentiation. Collectively, these findings underscore the therapeutic potential of developing chemical stabilizers for the PRDX1−DOK3 complex in suppressing plasma cell differentiation for RA treatment and establish a theoretical basis for targeting PRDX1-protein interactions as specific therapeutic targets in various diseases.

© 2025 The Authors. Published by Elsevier B.V. on behalf of Chinese Pharmaceutical Association and Institute of Materia Medica, Chinese Academy of Medical Sciences. This is an open access article under the CC BY-NC-ND license (http://creativecommons.org/licenses/by-nc-nd/4.0/).

1. Introduction

Rheumatoid arthritis (RA) is a systemic autoimmune disease with joint damage and disability. The prevalence of RA has shown a significant upward trend[1,2]. The pathogenesis of RA remains unknown, involving a complex interplay between environmental risk factors and genetic predisposition[2]. The primary focus of RA treatment revolves around achieving remission or maintaining low disease activity. RA is generally accompanied by producing autoantibodies, including rheumatoid factor (RF) and anti-citrullinated protein antibodies (ACPA)[3]. B cells are pivotal in the pathogenesis of RA, contributing to disease progression through antibody-dependent and independent functions[4,5]. Notably, the expansion of B cells observed in both peripheral blood and synovial tissue correlates with clinical outcomes[6,7]. Consequently, therapies targeting B cells have demonstrated efficacy in RA. There are various approaches, such as targeting B cell surface receptors (anti-CD20, anti-CD38, anti-CD40), modulating intracellular B cell signaling pathways (Bruton's tyrosine kinase (BTK) inhibitors), targeting B cell-related cytokines (TNF, IL-6, and JAK inhibitors)[8]. Despite the crucial role of B cells in RA pathogenesis, it is essential to note that not all B cells are pathogenic, such as regulatory B cells. Understanding the genetic alterations occurring during B cell differentiation and activation in RA can deepen our comprehension of its pathogenesis and guide the development of targeted therapeutic interventions.

Peroxiredoxins (PRDXs) are antioxidant proteins containing catalytic cysteine residues that remove hydrogen peroxide, alkyl hydroperoxides, and peroxynitrite[9]. Mammals possess six isoforms of PRDXs, which are categorized into three subclasses based on the number and location of the active cysteine residues: typical 2-cysteine PRDXs (PRDX 1−4), atypical 2-cysteine PRDX (PRDX5), and 1-cysteine PRDX (PRDX6)[10]. PRDX1 is primarily expressed in the cytosol and nucleus. Recent research has revealed additional functions of PRDX1 as a protein chaperone, regulating signaling molecules in addition to antioxidant enzymes[11-14]. Despite its involvement in various physiological processes such as lung injury, Th2-type allergic asthma, and atherosclerosis[15-18], PRDX1's role in inflammatory diseases remains poorly understood. Previous studies have demonstrated PRDX1's protective effect in various pathological processes, but its role as a protein chaperone in plasma cell differentiation has not yet been elucidated.

Protein−protein interactions (PPIs) form the foundation of all cellular processes. Identifying the interaction partners of proteins and deciphering the spatial structures of protein complexes are essential steps toward understanding the mechanisms underlying genetic and infectious diseases. The investigation into their interplay holds the potential for significant advancements in disease treatment[19,20]. The discovery of small molecules capable of modulating PPIs has long been of interest to the biomedical field[21-23]. There are available tools for identifying compounds that induce new (neo)-protein associations[20,24,25]. Given PRDX1's role as a protein chaperone, exploring its interaction partners and functions could advance the development of targeted interventions for RA.

In this study, we have uncovered the protective role of PRDX1 in the progression of RA. PRDX1 binds to DOK3, mitigating its degradation by inhibiting the autophagy−lysosome pathway in B cells, consequently suppressing plasma cell differentiation and autoantibody production. Additionally, our findings demonstrate that salvianolic acid B (SAB), a potent small molecular glue-like compound, enhances the PRDX1−DOK3 interaction and prevents disease progression by inhibiting plasma cell differentiation. Our findings suggest that PRDX1 stabilizes DOK3 by the autophagy−lysosome pathway, thereby inhibiting plasma cell differentiation. Enhancing the PRDX1−DOK3 interaction may serve as a potential therapeutic strategy against RA.

2. Materials and methods

2.1. Mice

Prdx1-OE and *Prdx1*$^{-/-}$ homozygous mice on C57BL/6 background were purchased from Gempharmatech (Nanjing, China) and were intercrossed with DBA/1 mice to produce the F1 generation, which were then intercrossed with DBA/1 mice to generate the F2 generation. Subsequently, the F2 mice were inbred to produce the F3 generation, which was further inbred to obtain the F4 generation. The F4 generation was then inbred to obtain F5

wild type (WT), *Prdx1*-OE, and *Prdx1*$^{-/-}$ male mice for CIA experiments. Mice were housed in the animal experiments center at the School of Pharmacy under controlled conditions with a room temperature of 23 ± 2 °C, a 12-h light/dark cycle, and unlimited access to water and food. All animal experiments were conducted according to the guidelines of the Experimental Animal Ethics Committee of the School of Pharmacy, Fudan University (approval number 2021-09-YL-SXY-93).

2.2. Cell culture

NALM-6 cells (ATCC, CRL-3273) were cultured in RPMI 1640 medium (BasalMedia, Shanghai, China) supplemented with 1% Penicillin/Streptomycin (meilunbio, Dalian, China) and 10% FBS (Gibco, Waltham, MA, USA). HEK-293T cells were cultured in high-glucose DMEM (BasalMedia) supplemented with 1% Penicillin/Streptomycin and 10% FBS. Splenic B cells were cultivated in ImmunoCult-XF B cell base medium (Stem cell, 100−0646, Vancouver, Canada) supplemented with 1% Penicillin/Streptomycin. All cell lines were grown at 37 °C with 5% CO_2. Cells were tested for mycoplasma using the MycoBlue Mycoplasma Detector (Vazyme, D101-01, Nanjing, China).

2.3. ScRNA-seq data collection and data preprocessing

The read count matrices for scRNA-seq data from RA patients and healthy donors (HC) with different tissues (PBMC or synovial) were downloaded from a public database as displayed in Supporting Information Table S1.

2.4. Unsupervised clustering

The Seurat package was used to perform the following analysis[26]. After quality control, the read count matrix was normalized using the LogNormalize method and scaled to the center. Subsequently, the FindVariableFeatures function was applied to identify the top 2000 high variable genes to prepare for dimension reduction using principal component analysis (PCA). Following the results of PCA, harmony was used to integrate all the samples from different studies. Specifically, considering different platforms (10 × Genomics and CelSeq2) in B cells, CCA was used to correct batches of samples from these different platforms. Finally, the appropriate PCs were tested for clustering using the specific resolution parameters, and UMAP was used to display the clustering results. Marker genes for each cluster or under different conditions were identified by applying the Find All Markers function in Seurat with parameters set as "min.pct = 0.25, logfc.threshold = 0.25, p_val_adj < 0.05".

2.5. Tissue distribution of clusters

The ratio of observed to expected cell numbers ($R_{o/e}$) for clusters in the HC and RA groups was calculated to quantify the enrichment of each cluster in a given status (HC or RA). The expected cell numbers for each combination of cell cluster and group were obtained from the chi-square test. A cluster was considered enriched if the $R_{o/e}$ ratio was greater than 1.

2.6. Differential expression analysis

To identify differentially expressed genes or evaluate the significant difference of one gene between two groups, we used the Wilcoxon test in R, with multiple hypothesis correction using the Benjamini-Hochberg procedure. Genes with adjusted *P* values less than 0.05 were considered differentially expressed. Additionally, the log2 fold change (log2 FC) for each gene was calculated by subtracting the log2-transformed mean count in each group.

2.7. Pathway analysis

Pathway analyses in B cells were conducted using the GSVA package[27]. The pathways, including 50 hallmark gene sets and 4384 genes, were downloaded from the Molecular Signatures Database (MSigDB)[28]. Differences between the HC and RA groups were calculated using a linear model offered by the limma package[29].

2.8. Trajectory inference

The Monocle (version 2.14.0) algorithm was used to infer the B cell differentiation trajectory in PBMC and gene expression along the trajectory[30]. First, the top 1000 signature genes were identified using the differential Gene Test function. Then, after dimension reduction and ordering of cells with the default parameters, the translational relationships were determined. The summation of scores from each pathway was reported.

2.9. Collagen-induced arthritis

7−8 weeks-old male DBA/1 mice were purchased from Slrc laboratory animal and were immunized subcutaneously at the base of the tail with Bovine type II collagen (Chondrex, 20022, Woodinville, WA, USA) emulsion with complete Freund's adjuvant (Chondrex, 7009). Twenty-one days later, the mice received subcutaneous booster injections with the same formulation of Bovine type II collagen. Arthritis scores in each paw were graded in a blinded manner according to the criteria described previously[31]. To study the treatment of SAB (CSNpharm, CSN12497, Chicago, IL, USA), mice were comparably assigned to the vehicle, tofacitinib citrate tablets (Pfizer, New York, NY, USA), and SAB-treated groups according to the severity at the disease onset. Immunized DBA/1 mice received intraperitoneal injections of PBS or SAB (15 mg/kg and 30 mg/kg). Tofacitinib was given to the mice by intragastric administration. The serum was subjected to calculate the concentrations of IgG2A using the Mouse anti-bovine type II collagen IgG2A antibody subtype ELISA kit with TMB (Chondrex, 20322T). The hindlimbs were harvested for micro-CT imaging and histopathological analysis. The spleen was harvested for flow cytometry and RNA-seq analysis.

2.10. Histopathology

The hindlimbs underwent fixation in 4% paraformaldehyde and were subsequently embedded in paraffin. Serial sections of the paw sections were prepared and subjected to hematoxylin and eosin (H&E) staining. The histological severity scores were determined in a blinded manner, as previously described[32].

2.11. Flow cytometry

Single-cell suspensions from mouse spleens were obtained by squeezing and filtering through 70-μm cell strainers. Fixable Viability Stain 700 was employed to label nonviable cells. Subsequently, the samples containing 100 μL single-cell suspensions were stained with the indicated antibodies in PBS supplemented

with 2% FBS for 30 min. Cells were washed and resuspended in PBS supplemented with 2% FBS. Data were acquired using the Beckman flow cytometer and analyzed employing CytExpert software (Beckman, Brea, CA, USA). Details regarding antibody fluorophores and clones are presented in Table S2.

2.12. RNA-seq data processing and analysis

FASTQC data obtained from the company underwent preliminary quality control. Subsequently, FASTQC was employed for low-quality data filtering and quality assessment. Transcriptional reads were mapped to the mouse genome (GRCm38) using the STAR RNA-seq aligner, and the transcripts of mapped genes were subsequently counted. Feature Count software was employed to recount the genes, resulting in the original expression matrix. To identify differentially expressed genes (DEGs), the expression of all mapped genes was calculated and analyzed utilizing limma. Significant differences were subsequently assessed using a false discovery rate cut-off value of 0.05. DEGs were utilized for KEGG (https://www.kegg.jp/) and GO (http://www.geneontology.org/) gene enrichment analysis to elucidate the function of distinct experimental groups. The aforementioned analysis was conducted using the Cluster Profiler function. Statistical differences between enriched terms and pathways were adjusted using the Benjamini-Hochberg (BH) multiple correction method, with a stringent P value threshold of ≤ 0.05.

2.13. Generation of the PRDX1 overexpressing cell line

HEK-293T (ATCC, CRL-1573) cells were seeded overnight in 10 cm dishes. Then, the pMSCV-Flag-h*PRDX1*-puromycin plasmids, along with packaging plasmids psPAX2 and pMD2.G, were co-transfected into HEK-293T cells using polyethylenimine (Life-iLab, AC04L092, Shanghai, China). After 48 and 72 h of virus production, the supernatant was collected, filtered, and concentrated. NALM-6 cells were seeded and infected with lentivirus supernatants supplemented with 10 μg/mL polybrene (HANBIO, HB-PB-500, Shanghai, China) for 24 h and then selected in 5 μg/mL puromycin (HANBIO, HB-PU-500).

2.14. Immunoblotting

Cells were lysed in RIPA lysis buffer (Beyotime, P0013B, Shanghai, China) supplemented with cocktail protease inhibitor (MedChemExpress, HY-K0012, NJ, USA) and Phosphatase Inhibitor Cocktail (Selleck, B15001, Houston, TX, USA). Protein concentration was determined with the BCA Protein Assay Kit (Thermo Fisher Scientific, 23225, Waltham, MA, USA). Equal amounts of cellular lysates were separated by SDS-PAGE, and then the proteins were transferred onto polyvinylidene fluoride membranes. Polyvinylidene fluoride membranes were blocked with 5% non-fat milk for 1 h at RT. Subsequently, the membranes were incubated with the corresponding primary antibody at 4 °C overnight. Next, the membranes were washed with TBST three times and incubated with the secondary antibodies at room temperature. Finally, the immunoblots were imaged using a Clinx GenoSens S2 system**.** The primary and secondary antibodies utilized in this study are listed in Table S2.

2.15. RT-qPCR

Total RNA was extracted from NALM-6 cells or sorted cells using VeZol Reagent (Vazyme, R401-01). RNA was purified using a spin column and collection tube (Sangon Biotech, B615012-0001, Shanghai, China). cDNA synthesis was performed using 1 μg of total RNA following the instructions provided with the HiScript II Q RT SuperMix for qPCR kit (Vazyme, R223-01). Following reverse transcription, qPCR was conducted utilizing ChamQ SYBR qPCR Master Mix (Vazyme, Q331-02/03) in a QuantStudio 6 Flex Real-Time PCR System (Thermo Fisher Scientific). Relative expression levels were quantified using the ΔΔCt method. The primers utilized in this study are as follows:

h*PRDX1*-F: CCACGGAGATCATTGCTTTCA
h*PRDX1*-R: AGGTGTATTGACCCATGCTAGAT
h*GAPDH*-F: ACAACTTTGGTATCGTGGAAGG
h*GAPDH*-R: GCCATCACGCCACAGTTTC
m*Dok3*-F: CTACCAGCAGCACGTAAAGTT
m*Dok3*-R: GTCCCAGCTTTCTAGCCGA
m*Gapdh*-F: GGGTCCCAGCTTAGGTTCAT
m*Gapdh*-R: CCCAATACGGCCAAATCCGT

2.16. IP-MS

Flag-PRDX1 was expressed in NALM-6 cells, and cell lysates were incubated with anti-flag M2 magnetic beads (Merck, M8823, Darmstadt, Germany) for 12 h. Subsequently, the beads were washed and subjected to mass spectrometry.

2.17. Plasmid construction and protein purification

The WT *PRDX1* and mutant (C52S, C83S, 1−175 aa) *PRDX1* genes were individually cloned into the E. coli expression vector pET28a (+). Expression was induced in LB medium containing 50 mg/mL kanamycin. Expression was induced by isopropyl-β-D-thiogalactopyranoside (IPTG) at 16 °C. Nickel columns (Cytiva, Marlborough, MA, USA) were used with the Akta Pure System (Cytiva) using buffer A (50 mmol/L Tris−HCl, 200 mmol/L NaCl, 1‰ β-mercaptoethanol) and buffer B (50 mmol/L Tris−HCl, 200 mmol/L NaCl, 1 mol/L imidazole, 0.5‰ β-mercaptoethanol) to purify the His-PRDX1 recombinant protein. The purified proteins were identified for purity by SDS-PAGE and Coomassie Brilliant Blue staining. The protein was then concentrated to 10 mg/mL in buffer C (20 mmol/L HEPES, 150 mmol/L NaCl).

To purify the mutant PRDX1 protein used for crystallization, the TEV (tobacco etch virus) enzyme was used to remove the His tag. The TEV enzyme-treated sample was loaded again into a nickel column to isolate the His tag from the mutant PRDX1 protein. The purified mutant PRDX1 was concentrated to 5.5 mg/mL for crystallization. The wild-type DOK3(1−330 aa) gene was cloned into the *E. coli* vector pGEX-6P-1 and expressed in LB medium containing 100 mg/mL ampicillin. Expression was induced by IPTG at 20 °C, and Glutathione *S*-transferase (GST) columns (Cytiva) were employed with the Akta Pure System (Cytiva), utilizing buffer A (50 mmol/L HEPES, 500 mmol/L NaCl, 0.5 ‰ β-mercaptoethanol) and buffer B (50 mmol/L HEPES, 500 mmol/L NaCl, 20 mmol/L reduced glutathione, 0.5 ‰ β-mercaptoethanol) to purify the GST Tag recombinant protein.

2.18. In vitro GST-pulldown

To investigate direct PPIs *in vitro*, pull-down assays were conducted using recombinant GST-tagged DOK3(1−330 aa) and His-tagged PRDX1 (WT). 5 μg of purified His-PRDX1 recombinant protein and 5 μg of GST-DOK3(1−330 aa) were added to 500 μL

of buffer (20 mmol/L Tris−HCL pH 7.4, 150 mmol/L NaCl, 2.5 mmol/L EDTA, 0.5% NP-40), then incubated overnight at 4 °C. Subsequently, GST-beads (Cytiva, 17527902) were added and incubated for 6 h at 4 °C with rotation. The supernatant was removed by centrifugation at 1300 rpm (Centrifuge, Eppendorf, Hamburg, Germany) for 3 min, and the GST-beads were washed three times with binding buffer. Subsequently, the GST-beads were resuspended in 50 μL of binding buffer, and the proteins were analyzed by Western blotting.

2.19. HDX-MS assay

Peptides were identified using tandem mass spectrometry (MS/MS) with a Fusion Orbitrap mass spectrometer (Thermo Fisher Scientific). Production spectra were acquired in data-dependent mode, and the top eight most abundant ions were selected for ion analysis during per scan event. MS/MS data files were analyzed using Proteome Discover 2.4 (Thermo Fisher Scientific) for high-confidence peptide identification. The PRDX1 protein used in HDX-MS contains the His-tag and TEV enzymatic site sequence: MGSSHHHHHHHHHSSGLVPRGSHMENLYFQG. The DOK3 (1−330 aa) protein contains the AVI-tag: GLNDIFEAQKIEWHE. The Peptide numbering shown in the Results section has been subtracted from the amino acid length of the tag portion.

HDX-MS analysis: A concentration of 8 μmol/L PRDX1 protein (20 mmol/L HEPES, pH 7.0, 150 mmol/L NaCl) was incubated with and without 28 μmol/L DOK3 protein (20 mmol/L HEPES, pH 7.0, 150 mmol/L NaCl) overnight at 4 °C. 4 μL of the incubation complex were mixed with 16 μL of exchange buffer containing D_2O (50 mmol/L HEPES, pH 7.0, 50 mmol/L NaCl and 2 mmol/L DTT). The incubation lasted for 5 min at 4 °C and was then quenched with a solution containing 1 mol/L TCEP and 100 mmol/L NaH_2PO_4 (pH 2.5). The quenched samples were immediately injected into the LEAP Pal 3.0 HDX platform. Samples were passed through an immobilized pepsin column (2 mm × 2 cm) at a flow rate of 120 μL/min. The target was digested into peptides and then captured on a C18 PepMap300 capture column (ThermoFisher, 163593), desalted, and passed through an ACQUITY UPLC BEH C18 Column 1.7 μm 2.1 mm × 50 mm (Waters Corporation, 186002350, Milford, MA, USA), with a linear gradient of 4%−40% CH_3CN and 0.3% formic acid, over 6 min. Sample handling, protein digestion, and peptide separation were conducted at 4 °C. Mass spectrometry data were obtained using a Fusion Orbitrap mass spectrometer (Thermo Fisher Scientific). Intensity-weighted average *m*/*z* centre-of-mass values were calculated for each peptide envelope and subsequently converted to percentage of deuterium incorporation. Statistical significance of HDX data at each time point was determined by unpaired *t*-tests, a procedure integrated into the HDX Workbench software, where corrections for reverse-exchange were automatically handled by fully deuterated controls during HDX Workbench analysis.

2.20. Data rendering

The HDX data obtained from overlapping peptides were aggregated into individual amino acid values by a residue averaging methodology. Briefly, for each residue, the deuterium incorporation values and peptide lengths from all overlapping peptides were collated. These deuterium incorporation values were then adjusted based on the inverse of the respective peptide lengths. Subsequently, the weighted deuterium incorporation values were averaged to yield a singular value for each amino acid. Notably, the initial two residues of each peptide, as well as prolines, were disregarded in the computations.

2.21. Protein thermal shift

His-PRDX1 (10 μmol/L), GST-DOK3 (10 μmol/L), 5 × Protein Thermal Shift dye (Invitrogen, Carlsbad, CA, USA) and buffer (20 mmol/L HEPES pH 7.0, 150 mmol/L NaCl) were added to each well of a 96-well plate, with a total volume of 20 μL per well. The 96-well plate was placed in the q-PCR instrument for plate reading. The SAB treatment experiments were conducted with a protein concentration to compound concentration ratio of 1:20, where the compound concentration was 200 μmol/L. After completing the addition of samples, the 96-well plate was transferred to the qPCR instrument for plate reading. Subsequently, the samples were slowly heated from 27 °C to 95 °C over 26 min, and the fluorescence signal value at each time point was recorded as the raw data. Protein Thermal Shift Software V1.1 was utilized to analyze the ΔT_m value and peak shape of the protein.

2.22. BLI interference assay

The Octet platform (ForteBio, Silicon Valley, CA, USA) is based on biological layer interferometry (BLI), which is utilized for the detection and analysis of biomolecular interactions. This study utilized the Octet platform to assess the affinity between PRDX1 and SAB, DOK3 and SAB, PRDX1 and DOK3(1−330 aa), and the ternary complexes of PRDX1, DOK3(1−330 aa), and SAB. Following the saturation fixation of DOK3(1−330 aa) protein using the Octet® Streptavidin (SA) Biosensor chip (Sartorius, Gottingen, Germany), analytes were diluted in a concentration gradient with buffer (20 mmol/L HEPES pH 7.0, 150 mmol/L NaCl, 0.02% Tween), and subsequently, the aforementioned samples and reagents were sequentially added to a black 96-well plate (Corning, NY, USA). Signals and data were processed using Octet program settings, and affinity values were calculated using Forte Data Analysis 9.0 software. All assays were conducted using the Octet Red96 instrument. AVI-tagged DOK3(1−330 aa) proteins were dissolved in a buffer (20 mmol/L HEPES pH 7.0, 150 mmol/L NaCl, 0.02% Tween) and immobilized on the SA sensor at a concentration of 10 μg/mL. Buffers without PRDX1 and empty SA sensors without immobilizing proteins were used as negative controls. When evaluating the affinity of recombinant proteins and SAB, AVI-tagged DOK3(1−330 aa) proteins and AVI-tagged PRDX1 proteins were immobilized on SA biosensors, respectively. Buffers without SAB and empty SA sensors without immobilizing proteins were used as negative controls. Baseline, immobilizing, association, and dissociation steps were timed at 120, 60, 180, and 300 s, respectively. They were fitted to a 1:1 binding kinetic model using ForteBio Data Analysis Software 9.0. The final figure was displayed using GraphPad (v8.0).

2.23. Protein crystallization and determination

The crystal of mutant PRDX1 protein ($PRDX1^{C52SC83S,1-175aa}$) was incubated in a well solution buffer containing 8% Tacsimate pH 5.7 (*v*/*v*), 20% PEG3350 (*v*/*v*), and 56% H_2O for 7 days at 18 °C. 1 μL of the protein solution was mixed with 1 μL of the well solution buffer and incubated in a seated drop plate. SAB was dissolved in the well solution buffer to a final concentration of 10 μmol/L. The well solution buffer containing 10 μmol/L of

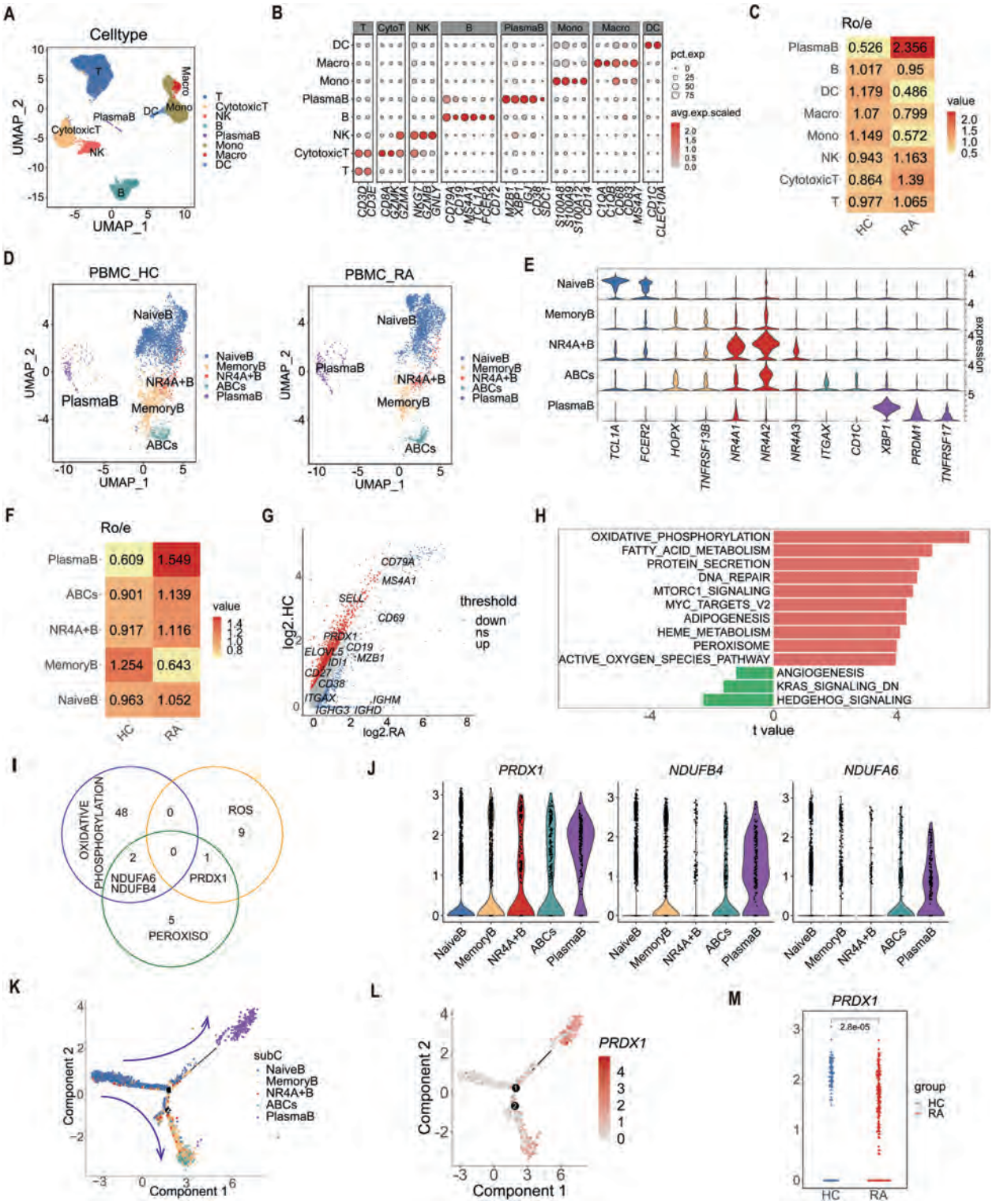

Figure 1 PRDX1 is downregulated in the plasma cells of RA. (A) UMAP visualization of the immune cells in PBMC from HC and RA. (B) A bubble heatmap depicting the expression levels of selected signature genes of various immune cells. Dot size indicates the fraction of expressing cells, colored based on scaled expression levels. (C) The enrichment of each immune cluster in HC and RA was estimated by a Ro/e score. (D) UMAP visualization of B cells in PBMC from HC and RA. (E) Expression levels of selected signature genes in various B cell subsets. (F) The enrichment of each B cell cluster in HC and RA was estimated by a $R_{o/e}$ score. (G) Volcano plots showing the significantly differentially expressed genes in HC and RA. Red dots indicate significantly upregulated genes, blue dots represent downregulated genes, and grey dots indicate no significant change. (H) Enriched pathways in HC compared to RA for B cells from PBMC, analyzed using GSVA. (I) Venn diagram showing genes involved in oxygen-related pathways. (J) Expression levels of PRDX1, NDUFA6, and NDUFB4 in B-cell clusters. (K) Developmental trajectory analysis of B-cell clusters. (L) PRDX1 expression levels along the trajectory of B-cell clusters. (M) The difference in expression of PRDX1 between HC and RA was analyzed using the Wilcoxon test.

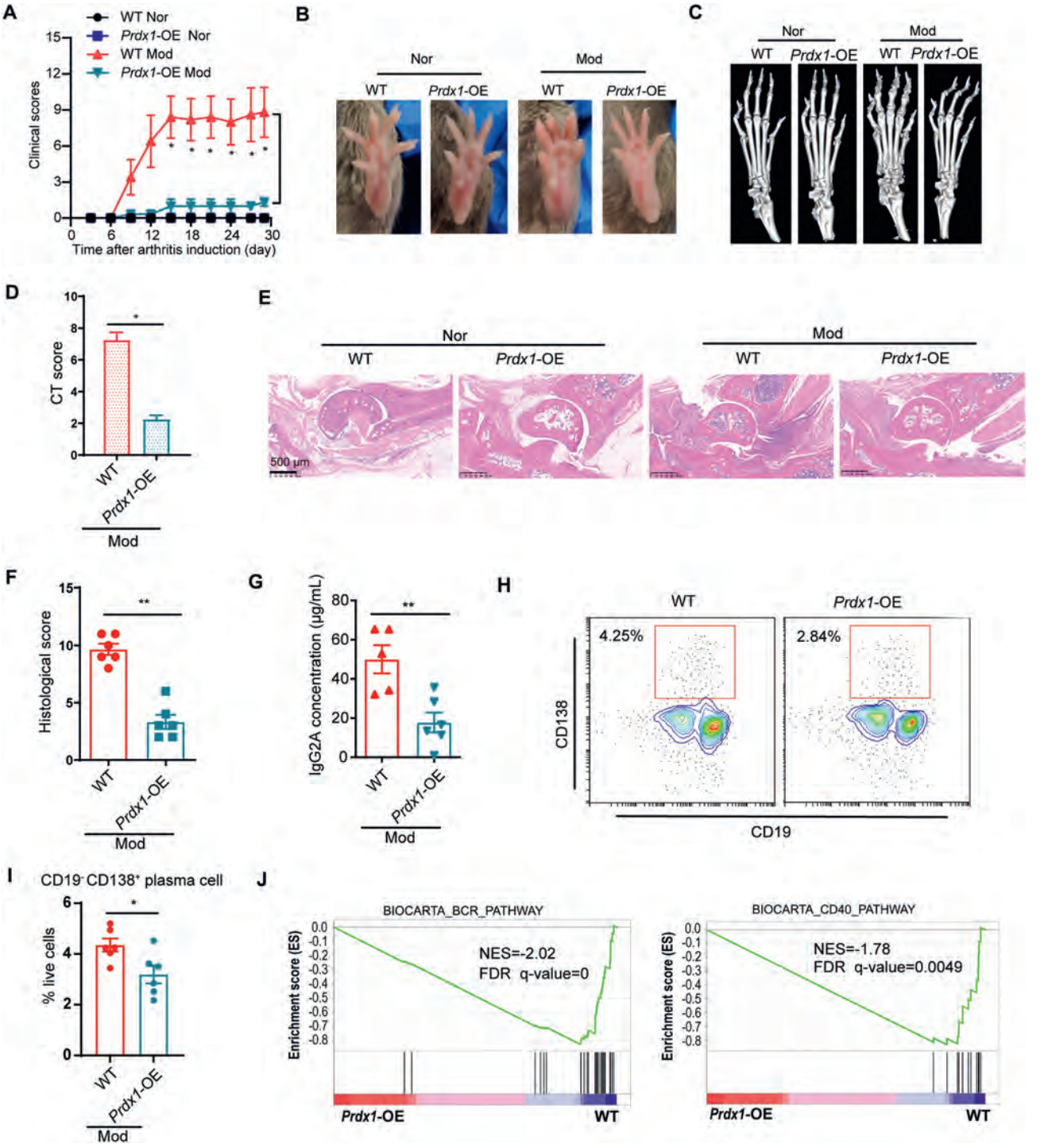

Figure 2 PRDX1-OE attenuates the disease progression of RA by inhibiting plasma cell differentiation. (A) The clinical arthritis severity score was assessed in WT and *Prdx1*-OE mice immunized with collagen in complete Freund's adjuvant ($n = 6$). (B) Representative images of paws from the WT and PRDX1-OE group. (C) Representative micro-CT images of paws from the WT and PRDX1-OE groups. (D) Joint destruction from the WT and PRDX1-OE groups was graded using CT score ($n = 3$). (E) Representative images of H&E-stained sections of ankle joints from the WT and PRDX1-OE groups are shown. Scale bar, 500 μm. (F) Histopathology analysis and histological scoring were performed on ankle joints from the WT and PRDX1-OE groups ($n = 6$). (G) Serum levels of IgG2A were analyzed by ELISA in WT and PRDX1-OE model groups ($n = 6$). (H) The proportion of plasma cells in the spleen was analyzed by flow cytometry. (I) A quantitative analysis of plasma cell counts in the spleens of *Prdx1*-OE and wild-type mice ($n = 6$). (J) GSEA enrichment profiles of the B cell receptor pathway and CD40 pathway in the spleens of *Prdx1*-OE and WT model mice. Data are shown as mean ± SEM, $^{*}P < 0.05$, $^{**}P < 0.01$, $^{***}P < 0.001$, $^{****}P < 0.0001$.

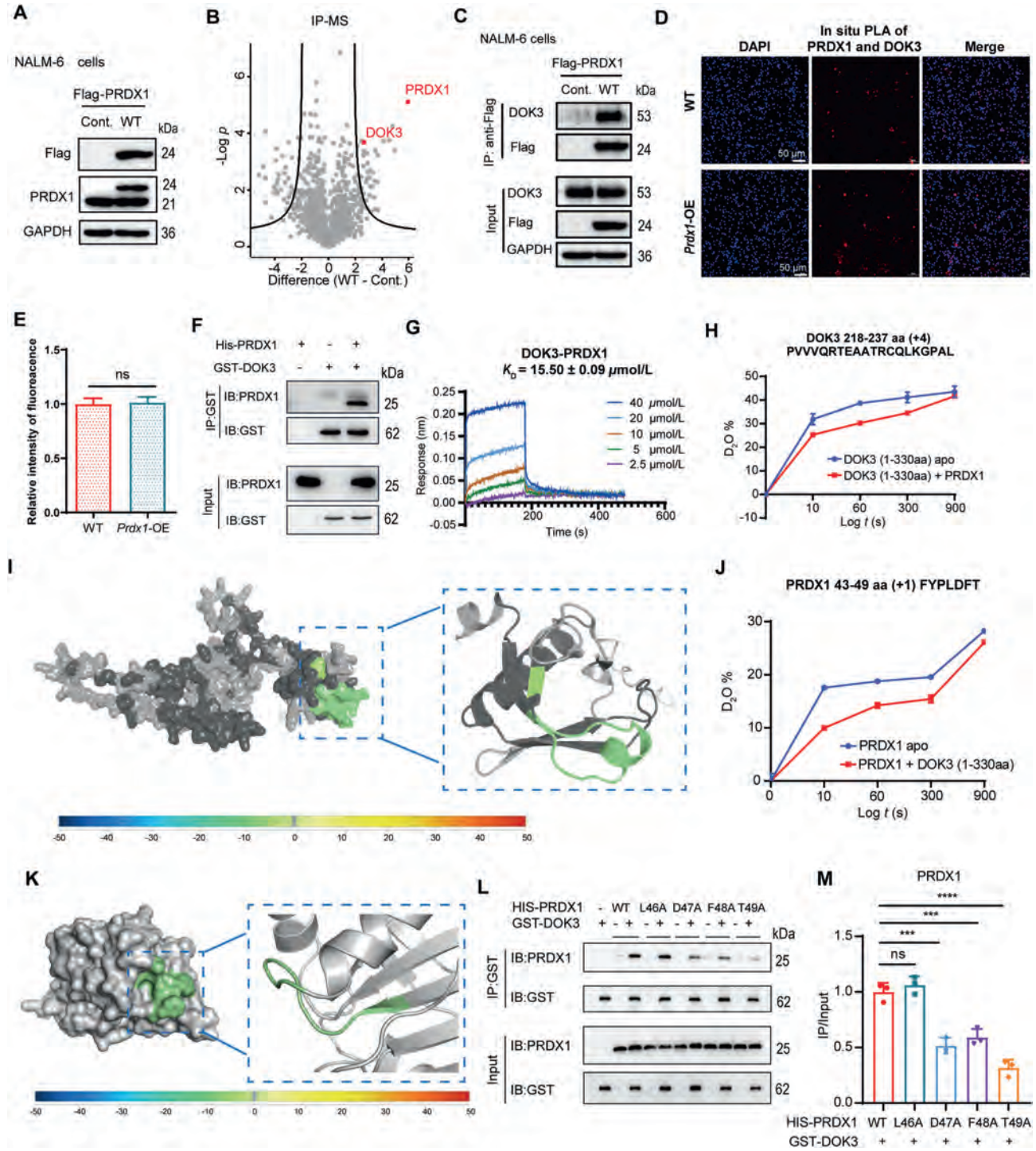

Figure 3 DOK3 serves as a PRDX1-interacting protein in B cells. (A) Immunoblots were performed in NALM-6 cells upon stable expression of PRDX1, with GAPDH serving as the loading control. (B) A volcano plot depicts differentially expressed proteins identified in co-immunoprecipitation assays of flag-PRDX1 in NALM-6 cells treated with anti-human CD40 antibody, human IL-21, and IL-4 for 48 h. (C) Co-immunoprecipitation of flag-PRDX1 in NALM-6 cells. (D) Representative images of Duolink *in situ* PLA using rabbit anti-PRDX1, mouse anti-DOK3 antibody, and PLA probes in WT and *Prdx1*-OE mouse B cells from the spleen. Scale bar, 50 μm. (E) Quantification of relative intensity of fluorescence in mouse WT and *Prdx1*-OE B cells using Duolink *in situ* PLA ($n = 3$). (F) Pull-down assay was performed using HIS-PRDX1 and GST-DOK3 in the purified form. (G) The interaction between His-PRDX1 and AVI-DOK3 was evaluated by BLI. K_D represents the dissociation constant ($n = 3$). (H) The Line graph shows deuterium uptake plots for peptide 218−237 aa of DOK3 in the presence and absence of PRDX1. (I) The 3D structure of DOK3(1−330 aa) was predicted using Alphafold to illustrate the perturbation of hydrogen−deuterium exchange upon interaction with recombinant PRDX1 protein. Peptide differences with % D between −5% and 5% were considered not significant and are shown in grey, while green−blue represents decreased hydrogen−deuterium exchange rate. Data are plotted as percentage deuterium uptake

compound was soaked with ligand-free PRDX1 crystals for 1 week at 16 °C. Before collecting X-ray data, the crystals were transferred to a cryoprotectant solution (containing 8% Tacsimate pH 8.0 (*v/v*), 20% PEG3350 (*v/v*), 18% glycerol), and then snap-frozen in liquid nitrogen. X-ray diffraction data were collected at the BL19U1 beamline at the Shanghai Synchrotron Radiation Facility (SSRF), integrated using the XDS package, and scaled using the Scala module of the CCP4 software. The structure was determined by molecular replacement using the Phaser module of the Phenix software, with the dimer of PRDX1 (PDB code: 4XCS) as the search template.

2.24. Cell sorting and in vitro stimulation of B cells

EasySep™ Mouse Pan-B Cell Isolation Kit (Stem Cell, 19844) was used to isolate pan B cells from single-cell suspensions of splenocytes through negative selection. Subsequently, B cells were washed with PBS. Next, B cells were plated at a concentration of 0.7×10^6 cells/mL in 24-well tissue culture plates and stimulated with anti-mouse CD40 antibody (2 μg/mL) (BD Pharmingen, 555586, Franklin Lakes, NJ, USA), murine IL-21 (50 ng/mL) (PeproTech, 210-21-10UG, Rocky Hill, NJ, USA) and IL-4 (50 ng/mL) (PeproTech, 214-14-20UG). The cells were passaged every 3 days.

2.25. Duolink assay

After *in vitro* stimulation of B cells, the Duolink assay was performed according to the manufacturer's instructions using Duolink Detection reagents Far Red (Sigma−Aldrich, St. Louis, MO, USA) and anti-PRDX1 rabbit (Proteintech, 15816-1-AP, Wuhan, China) and anti-DOK3 mouse primary antibodies (Santa Cruz Biotechnology, SC-390007, Santa Cruz, CA, USA).

2.26. Quantification and statistical analysis

GraphPad Prism 8 software was used to conduct the unpaired two-tailed Student's *t* test, one-way ANOVA, or Mann−Whitney test. The data are presented as means ± standard error of mean (SEM). The number of samples and independent experiments is indicated in each figure legend. A significance level of $P < 0.05$ was considered statistically significant.

3. Results

3.1. PRDX1 is downregulated in the plasma cells of RA

To investigate key cell populations and discover therapeutic targets, scRNA-seq data were downloaded and utilized[33-37]. After quality control and batch effect removal, 38405 immune cells from peripheral blood mononuclear cells (PBMCs) of RA patients and HC were clustered into eight main clusters with classic markers. These included three clusters of NKT cells-T ($CD3D^+$), cytotoxic T ($CD3D^+CD8A^+NKG7^+$) and NK ($CD3D^-NKG7^+$), two clusters of B cells ($CD79A^+$) and plasma B ($CD38^+$), and three clusters of Myeloid cells (LYZ^+)-Mono ($S100A^+$), Macro ($C1Q^+$) and DC ($CD1C^+$/$CLEC10A^+$) (Fig. 1A and B, and Supporting Information Fig. S1A). $R_{o/e}$ analysis[38] was conducted to quantify the cell type enrichment in RA and HC, revealing referential enrichment of Plasma B cells in RA patients (Fig. 1C). This aligns with the concept that RA initiation involves autoantibodies production and B cell depletion had beneficial effects on the clinical presentation[39]. Subsequently, the 9665 B cells from PBMCs and synovium of RA and HC subjects were collected and further annotated. In total, five clusters were identified: Naïve B ($TCL1A^+$ $FCER2^+$), $NR4A^+$ B ($NR4A^+$), ABCs ($ITGAX^+CD1C^+$), Memory B as a transient state between $NR4A^+$ B and ABCs ($HOPX^+ITGAX^+$), and Plasma B ($XBP1^+$ $SDC1^+$) (Fig. 1D, E, and Fig. S1B). Similar to previous findings, Plasma B cells were most enriched in RA patients' PBMC compared to other clusters (Fig. 1F). Given that gene expression can reflect phenotype and function, we compared the gene expression between RA and HC groups in B cells, identifying 1048 genes with significant expression difference (Fig. 1G). Comparison of gene expression in B cells between RA and HC groups revealed significant enrichment of oxygen-related pathways, such as oxidative phosphorylation, peroxisome, and ROS, as identified by gene set variation analysis (GSVA) (Fig. 1H).

Based on the oxidative stress affecting B cell activation and differentiation[40], our study focused on oxygen-related pathways to identify crucial targets in RA. Among the intersection genes in the oxygen-related pathways, PRDX1 exhibits significant changes (Fig. 1I and J). Pseudotime analysis of B cells revealed two distinct cell fates originating from Naïve B cells, one to Memory B cells and the other to Plasma B cells (Fig. 1K). Along this trajectory, the expression of PRDX1 increased, indicating higher expression in activated B cells (Memory B and Plasma B) (Fig. 1L, Fig. S1C and S1D). Further analysis showed that the PRDX1 expression was reduced in RA patients compared to HC in plasma B cells (Fig. 1M). Additionally, PRDX1 expression in synovium B cells varies among patients with different disease progressions, with lower expression observed in severe disease conditions (Fig. S1E−S1G). These findings suggest that PRDX1 acts as a potential protective factor in RA pathogenesis.

3.2. PRDX1-OE attenuates disease progression of RA by inhibiting plasma cell differentiation

To investigate the role of PRDX1 in the pathogenesis of RA, we generated overexpression of PRDX1 (PRDX1-OE) male DBA/1 mice (Supporting Information Fig. S2A) and performed the collagen-induced arthritis (CIA) experiment. After two immunizations with bovine Type II collagen solution, the clinical score of joint swelling in the paws was typically increased in one week. PRDX1-OE inhibited disease progression at the onset of arthritis (Fig. 2A and B). The animal micro-PET/CT system showed that PRDX1-OE significantly alleviated bone destruction and bone loss

versus time on a logarithmic scale. (J) The line graph shows the deuterium uptake profile of peptide 43−49 aa of PRDX1 in the presence and absence of DOK3. (K) Differential HDX consolidation view was mapped to the PRDX1 crystal structure (PDB ID: 7WET) to demonstrate hydrogen−deuterium exchange perturbations upon interaction of the recombinant PRDX1 protein and the recombinant DOK3(1−330 aa) protein. (L) Pull-down assay was performed using His-PRDX1mutants (L46A, D47A, F48A, T49A) and GST-DOK3 in the purified form. (M) Relative protein levels of His-PRDX1(Wild type and mutants) in the (L) pull-down assay ($n = 3$). Data are shown as mean ± SEM, $*P < 0.05$, $**P < 0.01$, $***P < 0.001$, $****P < 0.0001$, and ns indicates no significance.

(Fig. 2C and D). Histological analysis of paws in WT mice showed inflammatory cell infiltration, severe synovial proliferation, and cartilage destruction. These pathological changes were significantly ameliorated in *Prdx1*-OE mice (Fig. 2E and F). This was accompanied by decreasing IgG2A antibodies in serum (Fig. 2G) and a lower ratio of plasma cells in the spleen (Fig. 2H, I, and Fig. S2B). These findings suggest that PRDX1 may alleviate CIA by inhibiting plasma cell differentiation and antibody-induced inflammation.

To test the involvement of PRDX1 in CIA, we next performed RNA sequencing (RNA-seq) of the spleen from WT and *Prdx1*-OE model mice. Kyoto Encyclopedia of Genes and Genomes (KEGG) pathway enrichment analysis and Gene Ontology Biological Process (GO BP) showed that the B cell receptor signaling pathway and B cell activation were blocked in *Prdx1*-OE mice (Fig. S2C and S2D). The Gene Set Enrichment Analysis (GSEA) also showed enrichments for genes related to the B cell receptor signaling pathway and CD40 pathways in the WT model group (Fig. 2J), indicating that PRDX1-OE reduced both the B cell receptor signaling pathway and CD40 pathways. For functional validation of PRDX1 in B cells, we activated B cells obtained by magnetic bead sorting *in vitro*. We found that PRDX1 deletion increased the proportion of plasma cells (Fig. S2E and S2F), which is consistent with reduced antibody responses in *Prdx1*-OE mice. Collectively, these observations indicate that PRDX1 may negatively regulate plasma cell differentiation and exert a protective role in CIA pathogenesis.

3.3. DOK3 serves as a PRDX1-interacting protein in B cells

Based on PRDX1's function as a protein chaperone that regulates signaling molecules, PRDX1 may interact with B cell-associated proteins to engage in B cell activation and differentiation, independent of its classic antioxidant effects (Supporting Information Fig. S3A and S3B). To identify potential B-cell-associated proteins, we performed immunoprecipitation (IP) assays in overexpressed flag-PRDX1 NALM-6 cells with anti-flag beads (Fig. 3A and Fig. S3C). After IP assay and then mass spectrometry analyses, DOK3 protein was precipitated with flag-PRDX1 in NALM-6 cells upon anti-human CD40, human IL-4, and IL-21 stimulation (Fig. 3B). The adaptor protein DOK3 functions as a molecular scaffold to regulate signaling downstream of various immune receptors[41]. DOK3 is preferentially abundant in B cells and myeloid cells. In B cells, DOK3 plays an inhibitory role in B cell receptor signaling[42]. To determine the interaction between PRDX1 and DOK3 in cells, Co-IP assays were performed using anti-flag beads in *PRDX1*-OE NALM-6 cells and HEK-293T cells co-transfected with flag-PRDX1 and myc-DOK3. We observed that flag-PRDX1 could immunoprecipitate endogenous DOK3 in *PRDX1*-OE NALM-6 (Fig. 3C). Similarly, flag-PRDX1 could immunoprecipitate myc-DOK3 in HEK-293T cells (Fig. S3D). We also detected the interaction of endogenous PRDX1 and DOK3 in mouse WT and *Prdx1*-OE B cells by Duolink proximity ligation Assay (Fig. 3D and E). In addition, His-PRDX1 protein was also pulled down with the GST-DOK3 protein (Fig. 3F). Bio-Layer Interferometry (BLI) assay further demonstrated a direct interaction ($K_d = 15.50 \pm 0.09$ μmol/L) between His-PRDX1 and AVI-DOK3 (Fig. 3G).

Next, we investigated the interaction segments between PRDX1 (1−199 aa) and DOK3(1−330 aa) protein by the hydrogen−deuterium exchange mass spectrometry (HDX-MS) assay. The specific binding regions of PRDX1 and DOK3 interaction were colored according to different deuterium uptake rates. The green color denotes a decrease in exchange rate between amide hydrogen and deuterium, signifying tight binding regions between PRDX1 and DOK3. The protein segment analyzed for HDX-MS was DOK3(1−330 aa), encompassing the PH and PTB domains. Upon PRDX1 incubation, the PVVVQRTEAATRCQLKGPAL (218−237 aa) peptide segment of DOK3's PTB domain (Fig. 3H, I and Fig. S3E−S3G) showed reduced deuterium uptake, which means the interaction of PRDX1 and DOK3 enhanced solvent exchange protection of the peptide, indicating the peptide (P218−L237) is the specific binding region of DOK3 to PRDX1. Reduced deuterium uptake rates of PRDX1's FYPLDFT (43−49 aa) peptide revealed the importance of this region for their interaction, with an average 8.1% reduction compared to the control at all time points (Fig. 3J, K, and Fig. S3H−S3J). The pull-down assay of the PRDX1 mutation and DOK3 was conducted. The results indicated that the interaction between PRDX1 (L46A) and DOK3 exhibited no significant change compared to the wild-type protein. However, mutations in PRDX1 (D47A, F48A, T49A) led to a significant reduction in the interaction strength (Fig. 3L and M). Co-IP was performed in HEK-293T cells to further validate the results at the cellular level (Fig. S3K and S3L). Collectively, these findings indicate that PRDX1 interacts with DOK3 in B cells.

3.4. PRDX1 suppresses plasma cell differentiation by reducing the degradation of DOK3 in the autophagy−lysosome pathway

We investigated whether PRDX1 regulates B cell activation and differentiation through DOK3. DOK3 is a negative regulator of JNK signaling in B cells[42]. JNK is a subfamily of the canonical MAPK signal transduction pathway. To assess the importance of the PRDX1−DOK3 interaction, we examined the impact of DOK3 knockdown on plasma cell differentiation. Here, DOK3 knockdown significantly increased the proportion of plasma cells (Fig. 4A and B). Additionally, DOK3 knockdown significantly enhanced the JNK phosphorylation in B cells stimulated with anti-mouse CD40 and murine IL-21 and IL-4 (Fig. 4C and D). Compared with similarly treated WT B cells, PRDX1-OE B cells exhibited a significant reduction in JNK phosphorylation upon stimulation with anti-mouse CD40 and murine IL-21 and IL-4 (Fig. 4E and F). Interestingly, we observed an increase in DOK3 protein expression in *Prdx1*-OE B cells, while the mRNA level of DOK3 did not exhibit significant changes (Supporting Information Fig. S4A). Consistent with this, DOK3 protein was reduced in *Prdx1*$^{-/-}$ B cells in response to stimulation, accompanied by a significant increase in JNK phosphorylation (Fig. 4G and H). Additionally, Duolink proximity ligation assay revealed increased conjugation of DOK3 and PRDX1 in *Prdx1*-OE B cells (Fig. 4I and J). The GSEA revealed enrichments for genes related to MAPK signaling pathways in the WT model group, suggesting that the MAPK signaling pathway was suppressed in *Prdx1*-OE mice immunized with bovine Type II collagen solution. Furthermore, the GO-BP analysis indicated that the MAPK signaling pathway was inhibited in *Prdx1*-OE mice (Fig. S4B and S4C). Thus, these findings suggest that PRDX1 regulates DOK3 expression and the downstream signaling pathway in B cells.

DOK3 could be degraded in B cells treated with the anti-CD40 antibody and cytokines of IL-21 and IL-4 (Fig. 4K and L). We speculated that PRDX1 might be implicated in the regulation of DOK3 degradation. There are several possible mechanisms that degrade DOK3 protein, including the proteasome pathway and the

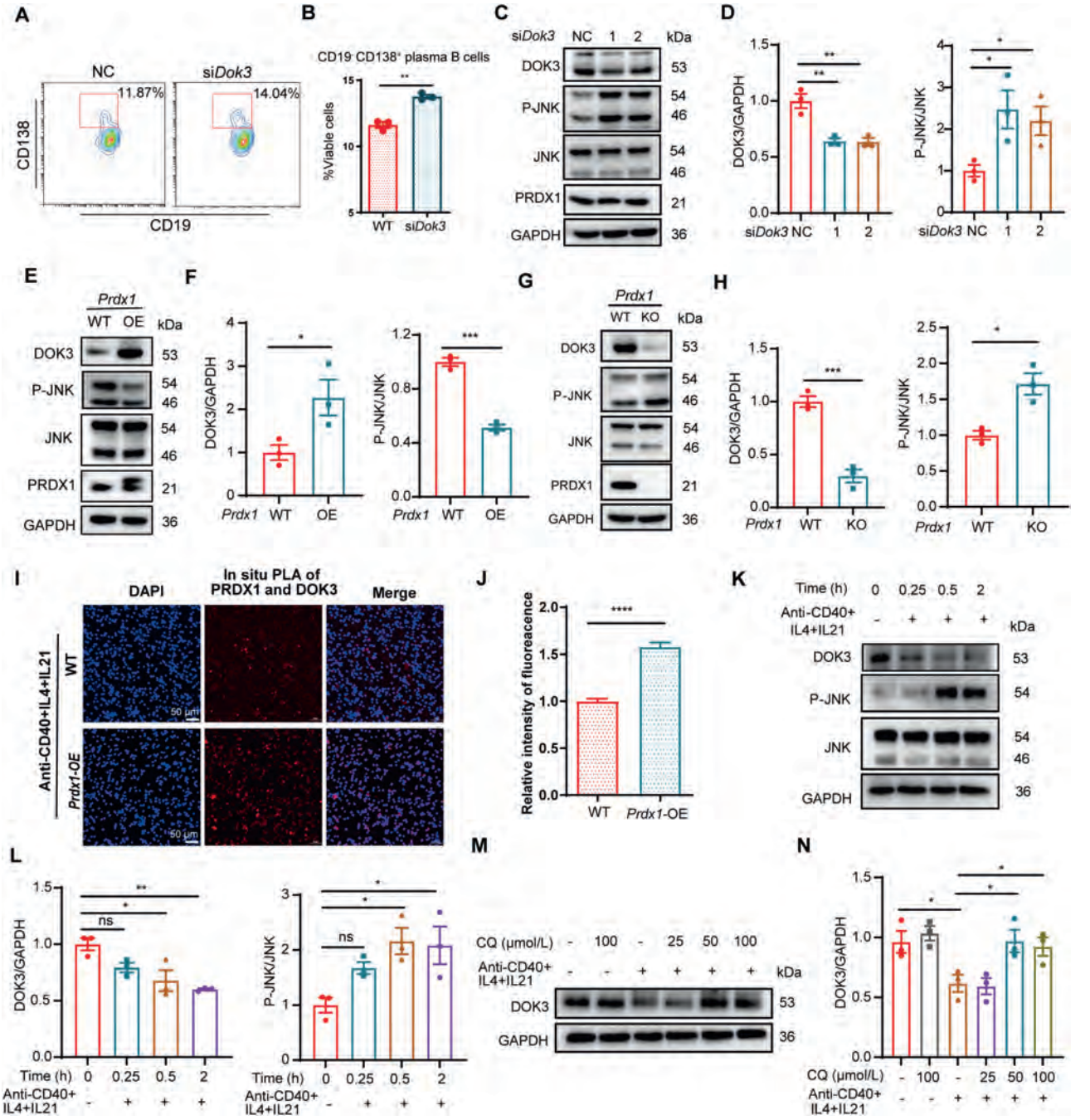

Figure 4 PRDX1 suppresses plasma cell differentiation by reducing the degradation of DOK3 in the autophagy−lysosome pathway. (A−D) WT B cells were treated with vehicle or siDOK3 and induced with anti-mouse CD40 antibody, murine IL-21, and IL-4. (A) The proportion of plasma cells was analyzed by flow cytometry. (B) A quantitative analysis of plasma cell counts in (A) ($n = 3$). (C) Immunoblot analysis was performed to assess the efficiency of DOK3 knockdown and JNK phosphorylation. (D) Relative protein levels of DOK3 and P-JNK in the (C) ($n = 3$). (E−H) Representative Western blot showing DOK3, phosphor-JNK, total JNK, and PRDX1 expression in WT, *Prdx1*-OE (E), and *Prdx1*$^{-/-}$ B cells (G) treated with anti-mouse CD40 antibody, murine IL-21, and IL-4 for 5 days, with GAPDH as a loading control. (F, H) Relative protein levels of DOK3, phosphor-JNK in WT, *Prdx1*-OE and *Prdx1*$^{-/-}$ B cells ($n = 3$). (I) Representative images of Duolink *in situ* PLA using rabbit anti-PRDX1, mouse anti-DOK3 antibody, and PLA probes in B cells from the spleen of the WT and *PRDX1*-OE mice, followed by anti-mouse CD40 antibody, murine IL-21, and IL-4. Scale bar, 50 μm. (J) Relative intensity of fluorescence of Duolink *in situ* PLA in B cells from the spleen of the WT and *Prdx1*-OE B cells ($n = 3$). (K) WT B cells were stimulated with anti-mouse CD40 antibody, murine IL-2, and IL-4 for the indicated times, and immunoblot analysis was performed to assess DOK3 and JNK phosphorylation. (L) Relative protein levels of DOK3 and P-JNK in WT B cells stimulated with anti-mouse CD40 antibody, murine IL-21, and IL-4 for the indicated times ($n = 3$). (M) WT B cells were treated with the lysosome inhibitor CQ following stimulation with anti-mouse CD40 antibody, murine IL-21, and IL-4 for 2 h, and immunoblot analysis was performed to assess DOK3. (N) Relative protein levels of DOK3 in WT B cells treated with the lysosome inhibitor CQ ($n = 3$). Data are shown as mean ± SEM, $^{*}P < 0.05$, $^{**}P < 0.01$, $^{***}P < 0.001$, $^{****}P < 0.0001$, and ns indicates no significance.

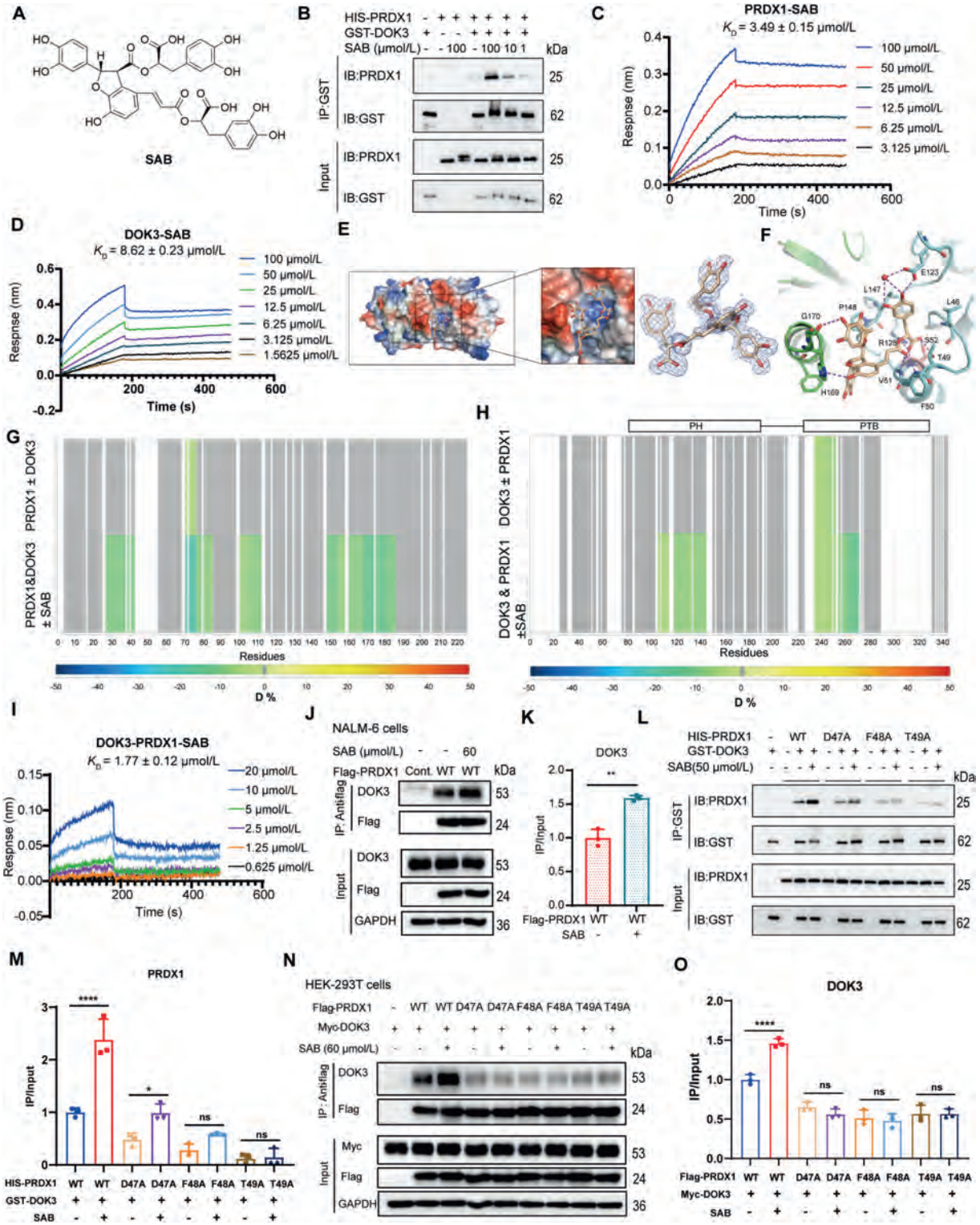

Figure 5 Salvianolic acid B functions as a molecular glue-like compound enhancing the interaction between PRDX1 and DOK3. (A) The chemical structure of salvianolic acid B is depicted. (B) Pull-down assay of GST-DOK3(1−330 aa) and His-PRDX1 protein incubated with 100, 10, and 1 μmol/L salvianolic acid B, respectively. (C) The binding affinity of AVI-PRDX1 with SAB was measured using a BLI binding kinetic assay. K_D stands for the dissociation constant (n = 3). (D) The binding affinity of AVI-DOK3(1−330 aa) with SAB was measured using a BLI binding kinetic assay. K_D stands for the dissociation constant (n = 3). (E) Electrostatic potential of the SAB−PRDX1 complex crystal structure and the binding site of SAB. The interior of SAB's binding site is electronegative (colored in blue), while its exterior is electropositive (colored in red). SAB was shown in the wheat stick. Unbiased F_o−F_c density map contoured at 2.5 Å of a crystal structure for PRDX1 in complex with SAB. (F) The hydrogen bond network formed between SAB and residues of PRDX1 is shown. The hydrogen bond network consists of ten hydrogen bonds, displayed as magenta dashed lines, while water molecules are represented as red spheres. (G) HDX analysis of PRDX1 comparing

lysosome pathway. We analyzed the effect of the proteasome inhibitor MG132 and the lysosome inhibitor chloroquine (CQ) on DOK3 protein levels in B cells treated with anti-CD40 antibody and cytokines IL-21 and IL-4. We observed that CQ treatment could stabilize DOK3 protein in these cells (Fig. 4M and N), indicating that DOK3 protein could be degraded by the lysosome pathway. At the same time, MG132 treatment had no significant effect on DOK3 protein levels in stimulated B cells (Fig. S4D and S4E). Recent studies have revealed that PRDX1 negatively regulates NF-κB activation and autophagy functions by inhibiting TRAF6 ubiquitin-ligase activity[12]. Therefore, we examined whether PRDX1 hindered the degradation of DOK3 by inhibiting the autophagy−lysosome pathway in B cells. Interestingly, PRDX1-OE increased the autophagy-associated protein LC3B lipidation upon stimulation (Fig. S4F and S4G), indicating inhibition of the autophagy-lysosome pathway in B cells. Therefore, these results demonstrate that the interaction of PRDX1 with DOK3 induces attenuation of DOK3 degradation, leading to inhibition of plasma cell differentiation.

3.5. Salvianolic acid B functions as a molecular glue-like compound enhancing the interaction between PRDX1 and DOK3

We further explored whether small molecules that enhance interaction between PRDX1 and DOK3 could inhibit plasma cell differentiation and alleviate RA disease severity. Given that we recently found PRDX1 could be potential target protein of some phenolic acid compounds, we tested some phenolic acids for the interaction of PRDX1 with DOK3 using the pull-down assay, such as salvianolic acid A, salvianolic acid B, salvianolic acid C, sodium danshensu, chlorogenic acid, tyrosol, and salicylic acid (Supporting Information Fig. S5A). Among these compounds, we found SAB significantly exhibited the most pronounced enhancement of the interaction between PRDX1 and DOK3 (Fig. 5A and B). In addition, BLI assay demonstrated the affinity of SAB with PRDX1 protein and DOK3(1−330 aa) protein was 3.49 ± 0.15 μmol/L and 8.62 ± 0.23 μmol/L, respectively (Fig. 5C and D). Subsequently, the protein thermal shift assay also showed a high affinity of SAB with PRDX1 protein (ΔT_m = 7.26 ± 0.05 °C) and DOK3 protein (ΔT_m = 2.00 ± 0.12 °C) (Fig. S5B and S5C). The complex crystal structure of SAB with PRDX1$^{C52SC83S,M1\text{-}A175}$ also showed that SAB bound at PRDX1 (Fig. 5E and Supporting Information Table S3). The complex crystal structure showed that both the F_o-F_c (Fig. 5F) and $2F_o-F_c$ (Fig. S5D) electron density maps of SAB remained intact and reliable. Ten hydrogen bonds between SAB and PRDX1$^{C52SC83S,M1\text{-}A175}$ formed a hydrogen bond network, which contains T49 (Fig. 5F).

Next, the HDX-MS assay was used to explore the interaction fragment of the ternary complex of SAB, PRDX1, and DOK3. The changes in deuterium uptake rates of DOK3 and PRDX1 treated with SAB respectively suggested SAB bound to the PRDX1 and DOK3 separately (Fig. S5E−S5H). Moreover, comparing PRDX1 and DOK3 binary complex before and after incubation with SAB, the color of the binary original binding regions deepens, and the green color of the ternary's binding region increases, which indicates that SAB promoted the binding of PRDX1 and DOK3 (Fig. 5G and H). Specifically, region I (2−15 aa), II (43−58 aa), III (73−85 aa), and IV (122−159 aa) of PRDX1 showed enhanced protection against solvent exchange after adding SAB to the PRDX1−DOK3 binary complex (Fig. S5I and S5J), in which region II is the original binding peptide of PRDX1 and DOK3 interaction as illustrated in Fig. 3. These regions exhibited at least a 7% reduction in deuterium uptake upon SAB enhancing DOK3 binding to PRDX1. Correspondingly, in HDX analysis of DOK3 (1−330 aa), the addition of SAB resulted in a greater reduction in hydrogen−deuterium exchange rate and increased protection against solvent exchange compared to the binary complexes. Region I (90−130 aa) and II (220−256 aa) also showed enhanced protection against solvent exchange, with deuterium uptake reduced at least 5% (Fig. S5K and S5L). The HDX-MS data suggest that SAB enhances the interactions between PRDX1 and DOK3. In addition, comparing binding affinity of DOK3−PRDX1 protein (K_d = 15.50 ± 0.09 μmol/L), SAB also enhanced the interaction of PRDX1 and DOK3 (K_d = 1.77 ± 0.12 μmol/L) (Fig. 5I). Subsequently, we detected the effects of SAB on the interaction between PRDX1 and DOK3 in NALM-6 cells. Notably, SAB treatment also enhanced the PRDX1 binding at DOK3 by Co-IP assay (Fig. 5J and K).

To better demonstrate how SAB enhances the interaction of PRDX1 and DOK3, mutations of PRDX1 were constructed. Based on the binding mode of SAB in the crystal structure and binding regions indicated by HDX-MS analysis, we found that the LDFT (46−49 aa) peptide of PRDX1 might play a crucial role in the interaction enhancement of SAB to PRDX1 and DOK3. Therefore, sequential mutations of this peptide were carried out. Indeed, SAB showed no hydrogen bond interaction with L46 in the crystal structure.

SAB was added to the pull-down assay of the PRDX1 mutants (D47A, F48A, T49A) to assess whether mutations at the binding sites between PRDX1 and DOK3 could neutralize the effects of SAB on the enhancement of the interaction. After the mutation of the corresponding sites, the enhancing effect of SAB on their interaction was attenuated (Fig. 5L and M). Co-IP assays conducted in HEK-293T cells further suggested that PRDX1 mutants (D47A, F48A, T49A) exert a crucial function in SAB, enhancing the interaction between PRDX1 and DOK3 (Fig. 5N and O). Taken together, these results demonstrate SAB functions as a molecular glue-like compound, enhancing PRDX1−DOK3 interactions *in vitro* and cells.

deuterium exchange rates before and after incubation with DOK3(1−330 aa) and after incubation of PRDX1 and DOK3(1−330 aa) with and without the addition of SAB. (H) HDX analysis of DOK3(1−330 aa) was performed to compare the rate of deuterium exchange before and after incubation with PRDX1, as well as the DOK3(1−330 aa) and PRDX1 complexes with SAB versus without SAB. (I) The affinity of the ternary complex of PRDX1, DOK3(1−330 aa), and SAB was measured by BLI binding kinetic assay. K_D stands for the dissociation constant (n = 3). (J) Co-immunoprecipitation of flag-PRDX1 in NALM-6 cells treated with 60 μmol/L SAB is shown. (K) The relative Protein levels of DOK3 in (J) (n = 3). (L) Pull-down assay was performed using GST-DOK3(1−330 aa) and His-PRDX1 mutant protein (D47A, F48A, T49A) incubated with 50 μmol/L salvianolic acid B. (M) Relative protein levels of His-PRDX1 (Wild type and mutants) in the (L) pull-down assay (n = 3). (N) The co-immunoprecipitation of flag-PRDX1 and its mutants wih myc-DOK3 in HEK-293T cells treated with 60 μmol/L SAB is shown. (O) The relative Protein levels of DOK3 in (N) (n = 3). Data are shown as mean ± SEM, *$P < 0.05$, **$P < 0.01$, ***$P < 0.001$, ****$P < 0.0001$, and ns indicates no significance.

3.6. Salvianolic acid B prevents the progression of collagen-induced arthritis by enhancing the interaction between PRDX1 and DOK3

Next, we investigated the effect of SAB on the immune responses of RA. SAB treatment started at the onset of CIA significantly reduced disease severity than control mice (Fig. 6A). SAB treatment did not significantly change the body weight of mice (Supporting Information Fig. S6A). The micro-CT and histological analysis also revealed that SAB could alleviate the bone destruction (Fig. 6B and C) and synovial inflammation (Fig. 6D and E). In addition, SAB also significantly inhibited the production of IgG2A antibodies (Fig. 6F), along with decreased plasma cell generation (Fig. 6G) and proportion of GC B cells in the spleen (Fig. 6H), accompanied by a similar frequency of total B cells in all groups (Fig. S6B). In addition, we investigated the effect of SAB on B cell activation and plasma cell differentiation in primary B cells. Upon stimulation with anti-CD40 antibody and cytokines (IL-21 and IL-4), the proportion of plasma cells increased in total B cells. SAB reduced the proportion of plasma cells compared with the control (Fig. S6D and S6E). However, after *Prdx1*$^{-/-}$ B cells were treated with SAB (10 μmol/L) in response to anti-CD40 and IL-21/IL-4 stimulation, the proportion of plasma cells did not significantly change (Fig. S6F and S6G).

To assess whether SAB also regulates B cell function, RNA-seq in the spleen from the model and SAB treatment was performed. GSEA revealed enrichments for genes related to BCR, CD40 signaling pathways, and the MAPK pathway in the model group (Fig. 6I, and Fig. S6C), suggesting that BCR, CD40 signaling pathways, and the MAPK pathway were inhibited upon SAB treatment. KEGG and GO-BP analyses revealed that compared with the model group, SAB treatment inhibits B cell activation and the BCR signaling pathway (Fig. 6J and K). Based on the above observation that SAB functioned as a molecular glue between PRDX1 and DOK3, we sought to explore the expression and co-localization of PRDX1 and DOK3 in the spleen from model and SAB treatment groups. Notably, SAB increased the interaction of the PRDX1−DOK3 and stabilized DOK3 protein (Fig. 6L and N). Fluorescence images of the spleen also revealed that the levels of P-JNK in the CIA group were higher than SAB treatment (Fig. 6M and O). Together, these results demonstrate that SAB serves as a PPI molecular glue to block degradation of DOK3 in the autophagy−lysosome pathway, and prevents the progression of collagen-induced arthritis by inhibiting plasma cell differentiation.

4. Discussion

Recent studies have extensively investigated the key cellular subsets involved in the pathogenesis of RA using both bulk and single-cell sequencing approaches. These studies have focused on various immune cell types, including CD4$^+$ T cells[43,44], B cells[35], monocytes[45], and fibroblasts[46], shedding light on the intricate cellular mechanisms underlying RA pathophysiology. The latest advancements provide a valuable opportunity to uncover essential pathways and therapeutic targets for RA. In our study, we employed a comprehensive single-cell analysis of PBMC and synovial immune cells from RA patients to identify potential regulators of B cell differentiation in RA pathogenesis. Our analysis revealed the activation of oxidative phosphorylation, peroxisome, and ROS pathways in B cells, underscoring their involvement in RA pathogenesis. PRDX1 has been identified as a key gene in the crosstalk within the oxidative-related pathway, exhibiting a significant alteration. Our research demonstrates that PRDX1 plays a potential negative regulatory role in plasma cell differentiation. Specifically, PRDX1-OE attenuated the progression of CIA and reduced the proportion of plasma cells along with antibody production. B cell differentiation is characterized by the expansion of the endoplasmic reticulum, accompanied by redox stress and reshaping of the antioxidant responses[47]. Although the current literature indicates that redox response contributes to orchestrating B cell differentiation, functional studies remain poorly understood. A recent study highlighted the significance of PRDX6 in B cells of systemic lupus erythematosus (SLE) patients, revealing its protective role against SLE by downregulating mitochondrial respiration and antibody production in B cells[48].

PRDX1, known as a molecular chaperone, is implicated in modulating the function of its binding proteins[49]. In our investigation, we demonstrated that PRDX1 interacts with DOK3 and suppresses plasma cell differentiation. DOK3 serves as an adapter molecule that negatively regulates immunoreceptor signaling in B cells[50]. Despite PRDX1's widespread expression in cells, it may exert specific regulatory effects on plasma cell differentiation through its interaction with DOK3 in B cells. Our findings highlight a specific peptide segment, PVVVVQRTEAATRCQLKGPAL, in the PTB domain of DOK3, which appears crucial for its interaction with PRDX1 (Fig. 3H). Moreover, our data demonstrated that PRDX1-OE inhibited the activation of the JNK pathway by reducing the degradation of DOK3, while PRDX1 knockout led to increased JNK phosphorylation and decreased DOK3 protein levels upon stimulation with anti-mouse CD40 antibody, murine IL-21, and IL-4. We further elucidate that PRDX1 hampered the DOK3 degradation by suppressing the autophagy−lysosome pathway specifically in B cells. In macrophages, previous research has shown that the E3 ligase TRAF6 is involved in the degradation of DOK3 during stimulation with CpG[51]. Additionally, LPS treatment induces DOK3 ubiquitination and degradation, leading to ERK activation[52]. However, the degradation of DOK3 in B cells has not been previously described. Our results suggest that the DOK3 degradation process in B cells is independent of proteasomal degradation, as MG132 treatment had no significant effect on the DOK3 protein levels. The autophagy-lysosome pathway appears to be uniquely associated with DOK3 degradation in B cells. Although most studies have highlighted DOK3's negative regulation in BCR signaling, it has also been reported to play a positive role in B cell activation. Upon immunization with 4-hydroxy-3-nitrophenyl-acetyl (NP) conjugated to chicken gamma-globulin (NP_{38}-CGG), DOK3 knockout B cells fail to sustain PDL1 expression and up-regulate PDL2, thereby facilitating plasma cell differentiation[53]. The modulation of B cell differentiation by DOK3 may vary across pathological contexts. Enhancing the interaction between PRDX1 and DOK3 to stabilize DOK3 protein may have diverse implications in different diseases. Moreover, considering the abundance of DOK3 in myeloid cells, the PRDX1−DOK3 complex may also regulate macrophage activation and osteoclast formation.

In our investigation, we have identified SAB as a molecular glue that enhances the interaction between PRDX1 with DOK3 proteins. Our findings indicate that SAB directly bound to both PRDX1 and DOK3(1−330 aa) protein, as determined by BLI assay (Fig. 5C and D). Notably, comparing the binding affinity of the DOK3−PRDX1 protein complex alone ($K_D = 15.50 \pm 0.09$ μmol/L), the presence of SAB enhanced this interaction, as evidenced by a reduced

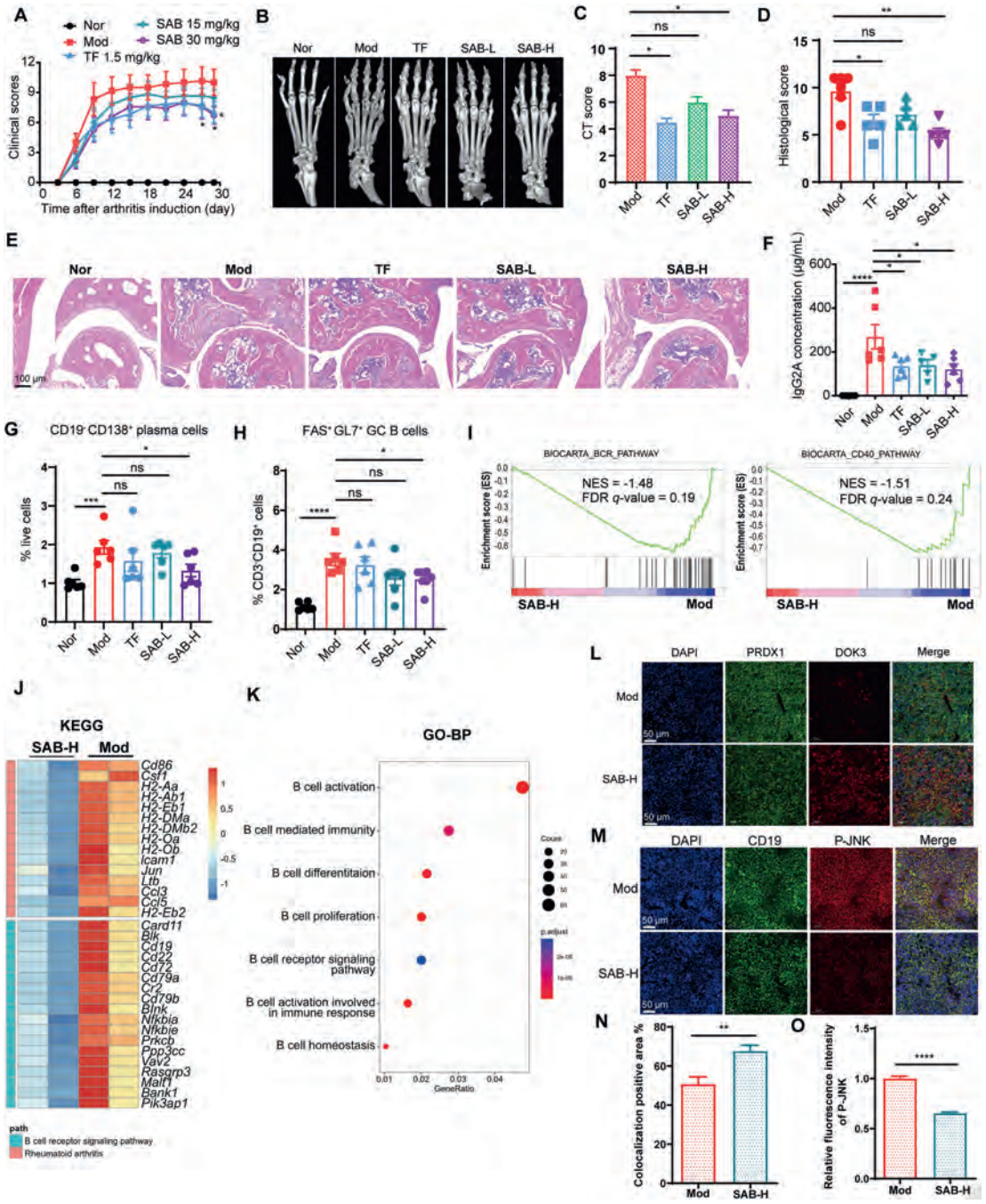

Figure 6 Salvianolic acid B prevents the progression of collagen-induced arthritis by enhancing the interaction between PRDX1 and DOK3. (A) Clinical scores of arthritis in mice treated with vehicle, 1.5 mg/kg TF, and 15 mg/kg or 30 mg/kg SAB, and immunized with collagen in complete Freund's adjuvant ($n = 6$). (B) Representative micro-CT images of the hind paws from mice treated with vehicle, TF, and SAB. (C) Joint destruction was graded based on the CT score in B ($n = 3$). (D, E) histological score of the inflammation area in mice treated with vehicle, TF, and SAB ($n = 6$) (D) and representative images of hematoxylin and eosin (H&E)-stained paw sections (E). Scale bar, 100 μm. (F) Serum titer of IgG2A analyzed from vehicle, TF, and SAB by ELISA ($n = 6$). (G, H) The frequency of plasma cells (G) and GC B cells (H) in the spleen from mice treated with vehicle, TF, and SAB was analyzed by flow cytometry ($n = 6$). (I) GSEA enrichment profiles of the B cell receptor pathway and CD40 pathway in the SAB-H treatment and model groups. (J) Heatmap depicting the expression levels of the B cell receptor signaling pathway and RA defined by the differentially downregulated genes in the SAB-H treatment group compared to the WT model group. (K) The biological process analysis of B cells for downregulated genes in the SAB-H treatment group compared to the model group. (L) Representative immunofluorescence staining images of PRDX1 (green) and DOK3 (red) in the spleen from the model and SAB treatment groups. Scale bar, 50 μm. (M) Representative immunofluorescence staining images of CD19 (green), P-JNK (red) in the spleen from the model and SAB treatment groups. Scale bar, 50 μm. (N) Relative fluorescence intensity of stained PRDX1 and DOK3 in the spleen from the model and SAB treatment groups ($n = 3$). (O) Relative fluorescence intensity of stained CD19 and P-JNK in the spleen from the model and SAB treatment groups ($n = 3$). Data are presented as mean ± SEM. $^{*}P < 0.05$, $^{**}P < 0.01$, $^{***}P < 0.001$, $^{****}P < 0.0001$, and ns indicates no significance.

dissociation constant (K_D = 1.77 ± 0.12 μmol/L) (Fig. 5I). Additionally, HDX-MS data further support the notion that SAB promotes the binding of PRDX1 and DOK3. Functionally, our study demonstrates that SAB administration prevents the progression of CIA by suppressing plasma cell differentiation. This effect is associated with the increased strength of the PRDX1−DOK3 interaction and stabilization of DOK3 protein levels in the spleen. Therefore, SAB acts as a protein−protein interaction molecular glue, impeding the degradation of DOK3 in B cells and consequently attenuating the progression of CIA by inhibiting plasma cell differentiation. Indeed, previous studies have shown that SAB possesses therapeutic potential in alleviating oxidative stress and inflammation in CIA rats and a mouse osteoarthritis[54,55]. However, the specific molecular targets of SAB have remained incompletely defined. Our results provide a rationale that SAB enhances the interaction between PRDX1 and DOK3 for RA therapeutic strategies. Currently, the salvianolic acid B magnesium injection, containing 80% salvianolic acid B, is clinically used to treat stable angina pectoris associated with coronary heart disease. Consequently, there is potential to extend its application to RA treatment.

5. Conclusions

Our study elucidates that PRDX1 interacts with DOK3, stabilizing it by suppressing the autophagy−lysosome pathway, which consequently inhibits plasma cell differentiation and alleviates the progression of collagen-induced arthritis. Additionally, we demonstrate that SAB acts as a molecular glue, enhancing the interaction between PRDX1 with DOK3 in B cells, thereby leading to the inhibition of plasma cell differentiation. These findings reveal that targeting the interaction between PRDX1 and DOK3 to inhibit plasma cell differentiation represents a promising therapeutic approach for RA.

Acknowledgments

We are extremely grateful to the National Centre for Protein Science Shanghai (Shanghai Science Research Center, Protein Expression and Purification system) for their instrument support and technical assistance. We thank the staff from BL17U1, BL18U1, BL02U1, and BL19U1 beamlines at Shanghai Synchrotron Radiation Facility (SSRF) for their assistance with our data collection. We also gratefully acknowledge the financial support by the National Key R&D Program of China (2022YFC3400500 and 2021ZD0203900 to Cheng Luo), the Strategic Priority Research Program of the Chinese Academy of Sciences (XDB0830300 to Cheng Luo, China), the National Natural Science Foundation of China (92253303, U23A20108 and 22337004 to Cheng Luo, 82273946 and 81803554 to Yuanyuan Zhang, 82104064 to Heng Xu, and 82304537 to Xiao Li), the project of National Multidisciplinary Innovation Team of Traditional Chinese Medicine supported by National Administration of Traditional Chinese Medicine (ZYYCXTD-202004 to Cheng Luo, China), the Science and Technology Commission of Shanghai Municipality (YDZX20233100004032 to Cheng Luo, 22ZR1474200 to Hao Zhang, China), the Applied Basic Research Foundation of Yunnan Province (202501BC070005 to Cheng Luo, China).

Author contributions

Cheng Luo, Yuanyuan Zhang conceptualized the study and supervised experiments. Wenzhen Dang, Xiaomin Wang, Heng Xu, and Huaying Li designed and performed the study. Huaying Li, Xinyu Li, Qiong Wu, and Hao Zhang analyzed the scRNA-seq data and RNA-seq. Xiaomin Wang, Yulin Yang and Siqi Huang performed the protein purification and biochemical experiments. Wenzhen Dang and Yixuan Xu performed the cellular and animal experiments. Hongru Tao and Xiao Li helped with animal experiments. Wenzhen Dang, Xiaomin Wang, and Huaying Li wrote the paper. Xiaoyan Shen and Lijiang Xuan analyzed results and provided reagents. Weilie Xiao, Dean Guo, Jie Zhen, and Kaixian Chen provided critical comments and suggestions. All authors read and contributed to the final manuscript.

Conflicts of interest

The authors declare no competing interests.

Appendix A. Supporting information

Supporting information to this article can be found online at https://doi.org/10.1016/j.apsb.2025.06.006.

References

1. Cao F, Liu YC, Ni QY, Chen Y, Wan CH, Liu SY, et al. Temporal trends in the prevalence of autoimmune diseases from 1990 to 2019. *Autoimmun Rev* 2023;**22**:103359.
2. Finckh A, Gilbert B, Hodkinson B, Bae SC, Thomas R, Deane KD, et al. Global epidemiology of rheumatoid arthritis. *Nat Rev Rheumatol* 2022;**18**:591−602.
3. Burgers LE, van Steenbergen HW, Ten Brinck RM, Huizinga TW, van der Helm-van Mil AH. Differences in the symptomatic phase preceding ACPA-positive and ACPA-negative RA: a longitudinal study in arthralgia during progression to clinical arthritis. *Ann Rheum Dis* 2017;**76**:1751−4.
4. Lee DSW, Rojas OL, Gommerman JL. B cell depletion therapies in autoimmune disease: advances and mechanistic insights. *Nat Rev Drug Discov* 2021;**20**:179−99.
5. Sun W, Meednu N, Rosenberg A, Rangel-Moreno J, Wang V, Glanzman J, et al. B cells inhibit bone formation in rheumatoid arthritis by suppressing osteoblast differentiation. *Nat Commun* 2018; **9**:5127.
6. Lu DR, McDavid AN, Kongpachith S, Lingampalli N, Glanville J, Ju CH, et al. T cell-dependent affinity maturation and innate immune pathways differentially drive autoreactive B cell responses in rheumatoid arthritis. *Arthritis Rheumatol* 2018;**70**:1732−44.
7. Qin Y, Cai ML, Jin HZ, Huang W, Zhu C, Bozec A, et al. Age-associated B cells contribute to the pathogenesis of rheumatoid arthritis by inducing activation of fibroblast-like synoviocytes *via* TNF-α-mediated ERK1/2 and JAK−STAT1 pathways. *Ann Rheum Dis* 2022;**81**:1504−14.
8. Wu F, Gao J, Kang J, Wang X, Niu Q, Liu J, et al. B cells in rheumatoid arthritis: pathogenic mechanisms and treatment prospects. *Front Immunol* 2021;**12**:750753.
9. Rhee SG, Kil IS. Multiple functions and regulation of mammalian peroxiredoxins. *Annu Rev Biochem* 2017;**86**:749−75.
10. Neumann CA, Cao J, Manevich Y. Peroxiredoxin 1 and its role in cell signaling. *Cell Cycle* 2009;**8**:4072−8.
11. Lv L, Bai J, Gao Y, Jin L, Wang X, Cao M, et al. Peroxiredoxin 1 interacts with TBK1/IKKε and negatively regulates pseudorabies virus propagation by promoting innate immunity. *J Virol* 2021;**95**:e0092321.
12. Min Y, Kim MJ, Lee S, Chun E, Lee KY. Inhibition of TRAF6 ubiquitin-ligase activity by PRDX1 leads to inhibition of NFKB activation and autophagy activation. *Autophagy* 2018;**14**:1347−58.
13. Hopkins BL, Nadler M, Skoko JJ, Bertomeu T, Pelosi A, Shafaei PM, et al. A peroxidase peroxiredoxin 1-specific redox regulation of the

novel FOXO3 microRNA Target let-7. *Antioxid Redox Signal* 2018;**28**: 62−77.
14. Park SY, Yu X, Ip C, Mohler JL, Bogner PN, Park YM. Peroxiredoxin 1 interacts with androgen receptor and enhances its transactivation. *Cancer Res* 2007;**67**:9294−303.
15. Yanagisawa R, Warabi E, Inoue K, Yanagawa T, Koike E, Ichinose T, et al. Peroxiredoxin I null mice exhibits reduced acute lung inflammation following ozone exposure. *J Biochem* 2012;**152**:595−601.
16. Kisucka J, Chauhan AK, Patten IS, Yesilaltay A, Neumann C, Van Etten RA, et al. Peroxiredoxin1 prevents excessive endothelial activation and early atherosclerosis. *Circ Res* 2008;**103**:598−605.
17. Lv WP, Li MX, Wang L. Peroxiredoxin 1 inhibits lipopolysaccharide-induced oxidative stress in lung tissue by regulating P38/JNK signaling pathway. *Eur Rev Med Pharmacol Sci* 2017;**21**:1876−83.
18. Inoue K, Takano H, Koike E, Warabi E, Yanagawa T, Yanagisawa R, et al. Peroxiredoxin I is a negative regulator of Th2-dominant allergic asthma. *Int Immunopharmacol* 2009;**9**:1281−8.
19. Seath CP, Trowbridge AD, Muir TW, MacMillan DWC. Reactive intermediates for interactome mapping. *Chem Soc Rev* 2021;**50**: 2911−26.
20. Durham J, Zhang J, Humphreys IR, Pei J, Cong Q. Recent advances in predicting and modeling protein-protein interactions. *Trends Biochem Sci* 2023;**48**:527−38.
21. Schreiber SL. The rise of molecular glues. *Cell* 2021;**184**:3−9.
22. Xiang H, Zhou M, Li Y, Zhou L, Wang R. Drug discovery by targeting the protein−protein interactions involved in autophagy. *Acta Pharm Sin B* 2023;**13**:4373−90.
23. Wu D, Li Y, Zheng L, Xiao H, Ouyang L, Wang G, et al. Small molecules targeting protein−protein interactions for cancer therapy. *Acta Pharm Sin B* 2023;**13**:4060−88.
24. Mason JW, Chow YT, Hudson L, Tutter A, Michaud G, Westphal MV, et al. DNA-encoded library-enabled discovery of proximity-inducing small molecules. *Nat Chem Biol* 2024;**20**:170−9.
25. Lucero B, Francisco KR, Liu LJ, Caffrey CR, Ballatore C. Protein−protein interactions: developing small-molecule inhibitors/-stabilizers through covalent strategies. *Trends Pharmacol Sci* 2023;**44**: 474−88.
26. Hao Y, Hao S, Andersen-Nissen E, Mauck 3rd WM, Zheng S, Butler A, et al. Integrated analysis of multimodal single-cell data. *Cell* 2021;**184**:3573. 87.e29.
27. Hänzelmann S, Castelo R, Guinney J. GSVA: gene set variation analysis for microarray and RNA-seq data. *BMC Bioinf* 2013;**14**:7.
28. Liberzon A, Birger C, Thorvaldsdóttir H, Ghandi M, Mesirov JP, Tamayo P. The Molecular Signatures Database (MSigDB) hallmark gene set collection. *Cell Syst* 2015;**1**:417−25.
29. Ritchie ME, Phipson B, Wu D, Hu Y, Law CW, Shi W, et al. Limma powers differential expression analyses for RNA-sequencing and microarray studies. *Nucleic Acids Res* 2015;**43**:e47.
30. Qiu X, Mao Q, Tang Y, Wang L, Chawla R, Pliner HA, et al. Reversed graph embedding resolves complex single-cell trajectories. *Nat Methods* 2017;**14**:979−82.
31. Fujimoto M, Serada S, Mihara M, Uchiyama Y, Yoshida H, Koike N, et al. Interleukin-6 blockade suppresses autoimmune arthritis in mice by the inhibition of inflammatory Th17 responses. *Arthritis Rheum* 2008;**58**:3710−9.
32. Li Y, Wang S, Wang Y, Zhou C, Chen G, Shen W, et al. Inhibitory effect of the antimalarial agent artesunate on collagen-induced arthritis in rats through nuclear factor kappa B and mitogen-activated protein kinase signaling pathway. *Transl Res* 2013;**161**:89−98.
33. Zhang F, Wei K, Slowikowski K, Fonseka CY, Rao DA, Kelly S, et al. Defining inflammatory cell states in rheumatoid arthritis joint synovial tissues by integrating single-cell transcriptomics and mass cytometry. *Nat Immunol* 2019;**20**:928−42.
34. Alivernini S, MacDonald L, Elmesmari A, Finlay S, Tolusso B, Gigante MR, et al. Distinct synovial tissue macrophage subsets regulate inflammation and remission in rheumatoid arthritis. *Nat Med* 2020;**26**:1295−306.
35. Meednu N, Rangel-Moreno J, Zhang F, Escalera-Rivera K, Corsiero E, Prediletto E, et al. Dynamic spectrum of ectopic lymphoid B cell activation and hypermutation in the RA synovium characterized by NR4A nuclear receptor expression. *Cell Rep* 2022;**39**:110766.
36. Sun D, Wang J, Han Y, Dong X, Ge J, Zheng R, et al. TISCH: a comprehensive web resource enabling interactive single-cell transcriptome visualization of tumor microenvironment. *Nucleic Acids Res* 2021;**49**:D1420−30.
37. Zhang B, Zhang Y, Xiong L, Li Y, Zhang Y, Zhao J, et al. CD127 imprints functional heterogeneity to diversify monocyte responses in inflammatory diseases. *J Exp Med* 2022;**219**:e20211191.
38. Zhang L, Yu X, Zheng L, Zhang Y, Li Y, Fang Q, et al. Lineage tracking reveals dynamic relationships of T cells in colorectal cancer. *Nature* 2018;**564**:268−72.
39. Smolen JS, Aletaha D, Barton A, Burmester GR, Emery P, Firestein GS, et al. Rheumatoid arthritis. *Nat Rev Dis Primers* 2018;**4**: 18001.
40. Raza IGA, Clarke AJ. B cell metabolism and autophagy in autoimmunity. *Front Immunol* 2021;**12**:681105.
41. Loh JT, Teo JKH, Lim HH, Lam KP. Emerging roles of downstream of kinase 3 in cell signaling. *Front Immunol* 2020;**11**:566192.
42. Ng CH, Xu S, Lam KP. Dok-3 plays a nonredundant role in negative regulation of B-cell activation. *Blood* 2007;**110**:259−66.
43. Stephenson W, Donlin LT, Butler A, Rozo C, Bracken B, Rashidfarrokhi A, et al. Single-cell RNA-seq of rheumatoid arthritis synovial tissue using low-cost microfluidic instrumentation. *Nat Commun* 2018;**9**:791.
44. Fonseka CY, Rao DA, Teslovich NC, Korsunsky I, Hannes SK, Slowikowski K, et al. Mixed-effects association of single cells identifies an expanded effector $CD4^+$ T cell subset in rheumatoid arthritis. *Sci Transl Med* 2018;**10**:eaaq0305.
45. Villani AC, Satija R, Reynolds G, Sarkizova S, Shekhar K, Fletcher J, et al. Single-cell RNA-seq reveals new types of human blood dendritic cells, monocytes, and progenitors. *Science* 2017;**356**:eaah4573.
46. Mizoguchi F, Slowikowski K, Wei K, Marshall JL, Rao DA, Chang SK, et al. Functionally distinct disease-associated fibroblast subsets in rheumatoid arthritis. *Nat Commun* 2018;**9**:789.
47. Bertolotti M, Yim SH, Garcia-Manteiga JM, Masciarelli S, Kim YJ, Kang MH, et al. B- to plasma-cell terminal differentiation entails oxidative stress and profound reshaping of the antioxidant responses. *Antioxid Redox Signal* 2010;**13**:1133−44.
48. Takeshima Y, Iwasaki Y, Nakano M, Narushima Y, Ota M, Nagafuchi Y, et al. Immune cell multiomics analysis reveals contribution of oxidative phosphorylation to B-cell functions and organ damage of lupus. *Ann Rheum Dis* 2022;**81**:845−53.
49. Rhee SG, Woo HA. Multiple functions of peroxiredoxins: peroxidases, sensors and regulators of the intracellular messenger H_2O_2, and protein chaperones. *Antioxid Redox Signal* 2011;**15**:781−94.
50. Lemay S, Davidson D, Latour S, Veillette A. Dok-3, a novel adapter molecule involved in the negative regulation of immunoreceptor signaling. *Mol Cell Biol* 2000;**20**:2743−54.
51. Liu N, Tang B, Wei P, Sun W, Wang S, Peng Q. TRAF6-mediated degradation of DOK3 is required for production of IL-6 and TNFα in TLR9 signaling. *Mol Immunol* 2015;**68**:699−705.
52. Peng Q, O'Loughlin JL, Humphrey MB. DOK3 negatively regulates LPS responses and endotoxin tolerance. *PLoS One* 2012;**7**:e39967.
53. Ou X, Xu S, Li YF, Lam KP. Adaptor protein DOK3 promotes plasma cell differentiation by regulating the expression of programmed cell death 1 ligands. *Proc Natl Acad Sci U S A* 2014;**111**:11431−6.
54. Xia ZB, Yuan YJ, Zhang QH, Li H, Dai JL, Min JK. Salvianolic acid B suppresses inflammatory mediator levels by downregulating NF-κB in a rat model of rheumatoid arthritis. *Med Sci Monit* 2018;**24**: 2524−32.
55. Lou Y, Wang C, Zheng W, Tang Q, Chen Y, Zhang X, et al. Salvianolic acid B inhibits IL-1β-induced inflammatory cytokine production in human osteoarthritis chondrocytes and has a protective effect in a mouse osteoarthritis model. *Int Immunopharmacol* 2017;**46**:31−7.